Relative-Entropy Variational Principle for Semiclassical Gravity with Finite-Resolution Boundaries

Olivier Nusbaumer *

Posted Date: 22 May 2026

doi: 10.20944/preprints202601.1205.v5

Keywords: quantum gravity; general relativity; semiclassical gravity; Wheeler-DeWitt; causal diamond; coherency screen; boundary completion; Hilbert space; non factorization; relative entropy; relative-entropic action; mismatch functional; variational principle; Kubo-Mori Metric; Hessian decoupling; block Diagonal Hessian; tensor sector; vector sector; scalar sector; topological budget; modular flow; KMS condition; modular locality; CPTP; GKSL; Lindblad; Lie filtration; Cartan subalgebra; Cartan torus; Heat-Kernel expansion; spectral trace; Gauss-Bonnet theorem; Euler characteristic; noncommutative geometry; spectral action; thermodynamic gravity; entropic gravity; holographic principle; emergent gravity; quantum information; quantum Fisher; Schur lemma; gauge topology; coherency units; Bekenstein-Hawking entropy; Yang-Mills; fine-structure constant; spectral tilt; tensor ratio; dark energy density; MOND scale; Higgs Mass; Top Quark Mass; Top Yukawa

Preprints.org (www.preprints.org) | NOT PEER-REVIEWED | Posted: 22 May 2026 doi:10.20944/preprints202601.1205.v5

Article

Relative-Entropy Variational Principle for Semiclassical Gravity with Finite-Resolution Boundaries

Olivier Nusbaumer

Leibstadt Nuclear Power Plant, 5325 Leibstadt, Switzerland; olivier.nusbaumer@kkl.ch or onusbaum@gmail.com

Abstract

This work formulates semiclassical gravity within a causal-diamond framework where a finite-resolution boundary provides the edge structure for a local Wheeler–DeWitt description. Because the diffeomorphism-invariant Hilbert space does not factorize, each diamond is equipped with a boundary-completed algebra $\mathfrak{A}_O$, ensuring the operational state ρ_O and the semiclassical reference family $\sigma_O[\Lambda]$ share identical operator content. Dynamics are posed as local statistical inference: the relative-entropy functional $S_{\mathrm{rel}}(\rho_O \| \sigma_O[\Lambda])$ quantifies the mismatch between data and reference. This yields the minimal operational axioms defining subsystems, intrinsic clocks, and regulated observables in a finite-resolution, background-independent setting. The topology-locked boundary capacity budget fixes an effective channel multiplicity $N \approx 1.23 \times 10^{11}$. Calibrating its coherent fraction to Newton's constant determines a matching scale $M_s \approx 3.02 \times 10^{13}$ GeV. In the modular/KMS regime, the relative-entropy Hessian (Kubo–Mori metric) block-diagonalizes into orthogonal tensor, vector, and scalar sectors. A quasi-local heat-kernel expansion on the fixed $S^3 \times S^1$ history manifold maps this near-equilibrium response to a matching-scale EFT, yielding the Einstein–Hilbert tensor structure, Yang–Mills susceptibilities, and leading mass deformations. Vector and scalar responses remain intensive, while the tensor response scales extensively. The reduced scalar-curvature sector fixes the R^2 plateau coefficient, equivalently locking the scalaron scale to $M_R = M_s$. The fixed modular protocol and quantized boundary currents give the matching-scale gauge condition $\alpha^{-1}(M_s) = 4\pi k$ for normalized current blocks. In the selected Standard Model boundary inventory this yields integer current levels for the strong and electromagnetic sectors, a weak-mixing projection, and a separate static electromagnetic susceptibility on $S^3 \times S^1$. The same boundary capacity gives linked plateau targets $n_s \simeq 0.965$, $r \simeq 0.0038$, and $A_s \simeq 2.1 \times 10^{-9}$, while single-pixel saturation gives electroweak-scale consistency checks for the Higgs, vacuum expectation, and top-sector scales. Translations between causal diamonds act as completely positive trace-preserving (CPTP) updates. The resulting open-modular Walsh filtration algebraically isolates a threefold matter-generation carrier and lepton-mass accessibility invariants. Treating continuum fields as the response of a finite boundary, the framework yields correlated, falsifiable relations for gravitational stiffness, gauge response, plateau cosmology, electroweak saturation, and threefold matter-sector organization from one minimal operational architecture.

Keywords: quantum gravity; general relativity; semiclassical gravity; Wheeler-DeWitt; causal diamond; coherency screen; boundary completion; Hilbert space; non-factorization; relative entropy; relative-entropic action; mismatch functional; variational principle; Kubo-Mori Metric; Hessian decoupling; block Diagonal Hessian; tensor sector; vector sector; scalar sector; topological budget; modular flow; KMS condition; modular locality; CPTP; GKSL; Lindblad; Lie filtration; Cartan subalgebra; Cartan torus; Heat-Kernel expansion; spectral trace; Gauss-Bonnet theorem; Euler characteristic; noncommutative geometry; spectral action; thermodynamic gravity; entropic gravity; holographic principle; emergent gravity; quantum information; quantum Fisher; Schur lemma; gauge topology; coherency units; Bekenstein-Hawking entropy; Yang-Mills; fine-structure constant; spectral tilt; tensor ratio; dark energy density; MOND scale; Higgs Mass; Top Quark Mass; Top Yukawa

1. Conceptual Foundations

We propose a finite-resolution framework for defining local quantum subsystems in semiclassical gravity, organized around the Wheeler–DeWitt (WDW) constraint [1]:

$$\hat{H}\Psi = 0$$

where the global state Ψ is constrained rather than time-evolved, and the operator $\hat{H}$ encodes gravitational constraints and diffeomorphism invariance.

To ensure background independence, we treat dynamics as local statistical inference on causal diamonds $\mathcal{O}(p,q)$ [2], the fundamental units of accessible correlations [3]. In the small-diamond regime, modular flow supplies the intrinsic local clock [4,5]. Geometry is inferred from an entropic mismatch functional between the actual boundary-completed state ρ_O and a semiclassical reference family $\sigma_O[\Lambda]$ defined by the background fields Λ [6–10].

The minimal architecture consists of a causal diamond equipped with boundary completion that stores the edge data required for a subregion algebra [2,11]. The resulting topological capacity functional defines an effective internal degeneracy N, and calibration to Newton's constant G fixes the matching-scale resolution M_s.

1.1. Axiomatic Basis: Minimal Architecture

In a background-independent theory, there is no external clock and no pre-existing global stage on which local observables are simply placed. Locality must therefore be defined operationally from the finite record accessible to an observer. The causal diamond provides the minimal covariant laboratory for this local inference [2], defined by two timelike-separated events and independent of global backgrounds.

Within this region, diffeomorphism and Gauss-law constraints obstruct naive bulk factorization, so subregion data must be tied to a closed boundary interface, the waist S^2. Holographic bounds require finite information capacity. Modular flow then supplies the intrinsic clock, boundary completion defines the measurable algebra, and finite resolution fixes the common operator content used to compare ρ_O with $\sigma_O[\Lambda]$.

Consequently, we formulate quantum gravity as local statistical inference in a background-independent, finite-resolution setting, bypassing a preferred lattice or pre-defined field content.

The axioms P1–P7 define the operational domain for subsystems, clocks and regulated observables. Topology, transport and spin structure then specify the minimal boundary sector, while constitutive relations calibrate its microscopic capacity to macroscopic gravity. Phenomenological results follow from this architecture.

The axioms are organized under three architectural principles:

Principle A: Operational Locality and Boundary Completion

Locality is defined operationally by the minimal covariant unit: a finite causal diamond [2]. This geometry fixes the boundary interface where subsystem-defining information must reside [11].

P1 (Non-factorization). The diffeomorphism-invariant physical Hilbert space does not factorize across spatial subregions ($\mathcal{H}_{\text{phys}} \neq \mathcal{H}_A \otimes \mathcal{H}_B$). Constraint relations tie interior data to boundary charges and fluxes, requiring explicit boundary data (edge modes) to define a well-specified subregion algebra [11–14].

P2 (Causal Diamonds). A finite experiment is a closed query–response loop between two timelike-separated events p and q. A causal diamond $\mathcal{O}(p,q) \equiv J^+(p) \cap J^-(q)$ [2] covariantly defines an observer's operational workspace. We restrict to the minimal simply connected sector: a maximal spatial slice of topology B^3 with a single closed waist S^2. This is the minimal local topology supporting a closed boundary completion (P3); nontrivial topologies require extra gluing data and lie outside the present analysis.

P3 (Boundary Completion). Since the physical Hilbert space does not factorize (P1), a well-defined subregion algebra $\mathfrak{A}_O$ requires boundary completion. States are positive, normalised functionals on $\mathfrak{A}_O$. This interface acts as a coherency screen at the diamond waist S^2, reconciling overlapping past and future boundary data into a unified record. We adopt a boundary-completed algebra whose finite-resolution centre $\mathcal{Z}(\mathfrak{A}_O)$ carries the gluing and charge labels needed to encode Gauss-law constraints. This ensures that ρ_O and $\sigma_O[\Lambda]$ live on identical operator content and define a common variational domain [11,13,15].

Principle B: Finite Modular Resolution

Finite capacity prevents unbounded boundary information density [16,17]. In the small-diamond KMS regime, modular flow supplies the intrinsic local clock [4,5,18].

P4 (Modular Locality). In the local Rindler regime the vacuum restricted to $\mathfrak{A}_O$ is approximately KMS with respect to a geometric modular flow. This applies in the small-diamond regime, where the diamond size is intermediate between the resolution limit and the local curvature radius. The modular Hamiltonian is well-approximated by the local boost generator, fixing KMS periodicity 2π [4,5].

Corollary (Canonical History Manifold). In the minimal simply connected sector, the two spatial B^3 domains associated with the causal-diamond halves glue across the waist as $B^3 \cup_{S^2} B^3 \simeq S^3$. The KMS condition evaluates local response on a compact Euclidean modular cycle S^1. The spectral trace is therefore represented on $S^3 \times S^1$, the minimal compact history manifold for this sector.

P5 (Finite Resolution). Defining a local subsystem requires finite resolution to ensure a stable restriction to $\mathfrak{A}_O$ and a bounded mode density at the interface. Since an algebraic restriction alone cannot fix the physical bandwidth, a proper-distance cutoff $L_s \equiv M_s^{-1} = \delta$ is introduced via a stretched screen in the local Rindler region. This finite-capacity regulator guarantees that ρ_O and $\sigma_O[\Lambda]$ admit a well-defined relative-entropy comparison, consistent with holographic bounds [16,19,20].

Corollary (Monotone Spectral Suppression). Relative entropy is monotone under the restriction of the accessible algebra (P3), while finite resolution imposes a strict limit on the information capacity per pixel (P5). In the resolved quasi-local regime, the infrared expansion is therefore organized in terms of intensive response densities and irrelevant corrections suppressed by powers of E/M_s. Extensive macroscopic quantities may grow with the total number of pixels, but the distinguishability available to each pixel remains bounded by the finite-capacity algebra.

Principle C: Quantized Boundary Topology and Minimal Transport

Non-factorization (P1) and boundary completion (P3) place charge labels on the boundary, represented here as discrete topological sectors [21]. Finite resolution supplies an isotropic transport layer for local excitations [22]. Near the sub-resolution tips, smooth modular flow must be routed through discrete boundary updates; the resulting digitization cost is the bottleneck that limits phase-coherent capacity.

P6 (Gauge Topology). Boundary charge sectors are encoded by topological current data compatible with non-factorization (P1) and closed algebraic gluing (P3). During one modular cycle, the causal-diamond waist sweeps out the closed boundary history $S^2 \times S^1$, whose current response is represented by a Chern–Simons functional [21]. With the trace normalization fixed, large gauge transformations of compact simple groups shift this functional by integer multiples of $2\pi k$; path-integral phase invariance therefore requires $k \in \mathbb{Z}$ [23]. Gauss law makes interior flux end on the spatial S^2 interface as representation-carrying punctures. These punctures generate surface states described by Wess–Zumino–Witten conformal blocks, equivalently chiral data organized by the affine Kac–Moody algebra at level k [24]. Retaining sectors compatible with KMS periodicity, large-gauge invariance, and anomaly inflow, this integer level fixes the boundary-current normalization entering the matching-scale inverse gauge coupling.

P7 (Discrete Isotropic Transport). A finite-resolution boundary architecture requires a local transport layer that is isotropic after modular averaging, inversion-symmetric, and compatible with spinorial matter. Modular closure requires that after a 2π period, local excitations return to their initial

Preprints.org (www.preprints.org) | NOT PEER-REVIEWED | Posted: 22 May 2026 doi:10.20944/preprints202601.1205.v5

states up to spin grading, lacking spurious phases or directional bias. Inversion symmetry pairs every transport direction with its opposite. The absence of directional bias requires the modularly averaged transport to be isotropic, so the second moment of the local step distribution is proportional to the identity. For three equal-length antipodal pairs with equal weights, this condition forces orthonormality, fixing the minimal transport layer to the signed basis $\{\pm x, \pm y, \pm z\}$, octahedral coordination $z = 6$, and the L_1 step rule. Supporting local spinors requires lifting $SO(3)$ to its double cover $SU(2)$, introducing a minimal $\mathbb{Z}_2$ grading. Since finite resolution (P5) provides the only intrinsic scale, we select a massless continuum transport operator that recovers local conformal covariance, removing arbitrary curvature-coupling ambiguities.

Corollary (Resolved Modular Interval and Lorentz Covariance). The cutoff $\delta \equiv M_s^{-1}$ is placed at fixed proper distance from the causal-diamond waist. Because the diamond is defined by light rays, this local placement introduces no preferred global frame. With local Rindler scaling $t \simeq \delta\tau$, the unresolved neighborhoods of the modular tips are excised, giving $\tau \in [\varepsilon, 2\pi - \varepsilon]$. The canonical screen placement sets $\varepsilon = 1$ in modular units. Nearby choices of ε rescale only the universal modular-window factor; the normalized coupling ratios remain fixed by the integer boundary-current levels. The discrete transport layer is confined to the boundary completion near the excised tips. Below M_s, the resolved interior is described by continuum fields on a smooth manifold; the leading EFT is locally Lorentz invariant, with regulator artifacts appearing only through irrelevant operators suppressed by powers of E/M_s.

Corollary (Minimal Regge-Transport Construction). Near the spacetime tips (p, q), the transverse cross-section falls below the resolution length $L_s = \delta$, forcing smooth L_2-isotropic modular flow to digitize onto the discrete L_1 transport layer. Here, an equal-weight signed router maps angular convergence onto an octahedral triangulation of the screen. At each of the six octahedral vertices, four equilateral triangular sectors meet; their angle sum is $4\pi/3$, giving a deficit $2\pi/3$ relative to the flat value 2π. The total deficit is therefore $6(2\pi/3) = 4\pi$, matching the Gaussian-curvature integral of the closed waist S^2 (equivalently 8π in scalar-curvature convention).

Corollary (Tip Defect Parameter κ). Routing continuous modular flow through the sub-resolution tips incurs an irreducible $L_2 \to L_1$ digitization overhead, encoded by the dimensionless boundary impedance κ. By P5, the resolved waist is a closed finite S^2 transport graph. Euler closure requires a net positive coordination deficit. In the selected minimal inversion-symmetric sector, this closure is realized by the octahedral router with three antipodal transport-axis pairs, $\{\pm x, \pm y, \pm z\}$. At each of the six octahedral poles, four equilateral triangular sectors meet. The Regge angular deficit is $2\pi - 4(\pi/3) = 2\pi/3$, so the normalized local defect fraction is $(2\pi/3)/(2\pi) = 1/3$. The six poles sum to 4π, giving the Gaussian-curvature closure of the sphere. Operationally, when a minimal unresolved update reaches a tip, isotropy forbids assigning it to a preferred transport axis. Its scalar effect is therefore distributed equally over the three independent axes, giving the spatial factor $1/3$. The remaining normalization comes from the intrinsic modular clock; the modular automorphism of the boundary algebra generates a KMS orbit with Euclidean period 2π. Thus, the per-tip leakage is the one-axis defect fraction averaged over one complete modular cycle: $\kappa = (1/3)(1/(2\pi)) = 1/(6\pi)$. A full causal-diamond modular cycle crosses both tips p and q, so the cycle-integrated leakage is 2κ.

Corollary (Transport-Orientation Redundancy $|\Gamma|$). The octahedral router contains three antipodal axis pairs, $\{\pm x, \pm y, \pm z\}$. Independent reversal of each orientation label generates $\Gamma \simeq (\mathbb{Z}_2)^3$, hence $|\Gamma| = 8$. These reversals act as equivalent sign conventions rather than propagating degrees of freedom. Under open modular evolution, they coarse-grain into commuting subalgebras (Chapter 2).

Corollary (Pixel). At finite resolution, a pixel represents a single resolvable algebraic patch on the boundary, defined by the triple $(\mathfrak{A}, \mathcal{H}, D)$ and represented by a node in the mesh. The local algebra $\mathfrak{A}$ acts on the internal fiber $\mathcal{H}$, while the transport operator D provides the nearest-neighbor connectivity routing data between adjacent nodes.

Corollary (Quantized Holographic Capacity). Octahedral transport admits compatible uniform subdivision by edge bisection. After n bisections, the number of resolved boundary patches scales as $V_n = 2 + 4^{n+1}$. The leading exponential growth is two-dimensional and area-like, while the invariant $+2$ term continuously records the Euler closure of the sphere. This realizes the boundary as a holographic area-scaling structure.

The axioms operate hierarchically. Axioms P1–P3 define the subsystem: a causal diamond completed by boundary data on a closed S^2 waist. Axioms P4–P5 supply the intrinsic modular clock and finite physical bandwidth. Axioms P6–P7 establish the minimal topological currents and isotropic transport required for gauge and spinorial data. Once the minimal sector is specified (one-tick resolution, octahedral transport, $\mathbb{Z}_2$ spin-twist, canonical normalizations) the subsequent structures, including S_{vac}, N, κ, N_{eff}, the Hessian blocks and the matching-scale EFT coefficients, arise as constrained outputs (rather than free continuous parameters).

1.2. Boundary Architecture, Resolution and Connectivity

A causal diamond $O(p, q)$ (P2) is bounded by two null hypersurfaces (future- and past-directed light-sheets) generated by null rays from p and q [2]. Their intersection defines a distinguished spacelike waist 2-sphere S^2, the maximal-area cross-section of the diamond. This waist serves as the local Rindler cut for the small-diamond description: it is the canonical interface on which a local subregion algebra can be completed when $\mathcal{H}_{\mathrm{phys}}$ does not factorize (P1–P3) [11,13]. This construction is purely local and does not rely on AdS asymptotics or an AdS/CFT embedding.

Finite resolution (P5) pixelizes the S^2 diamond waist into distinguishable patches at resolution δ, operationally aliasing sub-δ structures [19]. This replaces the idealized null interface in the local Rindler neighborhood with a stretched screen at proper distance δ [25]. The screen explicitly defines $\mathfrak{A}_O$ (P3), fixing the available edge observables and the common operator content shared by the actual state ρ_O and the reference family $\sigma_O[\Lambda]$.

Operationally, the null generators of the diamond act as update channels: the screen registers traversing excitations as discrete arrival events, supplying the raw record compared against $\sigma_O[\Lambda]$. The octahedral mesh on the S^2 waist represents this boundary sector, not a discretized bulk spacetime. The system is defined by graph adjacency, local transport rules and internal node labels.

In the local Rindler regime (P4), the local proper time at the screen scales as $t \simeq \delta\tau$ [5]. Identifying the minimal resolvable proper time with the screen resolution ($t_{\min} \sim \delta$) defines the canonical matching protocol $\varepsilon \equiv \tau_{\min} = 1$. Nearby choices of ε rescale the kinematic integration window uniformly across all gauge sectors. Thus the absolute normalization is tied to the canonical screen placement, while the integer-level ratios of inverse couplings remain topologically protected and depend only on the levels k_i.

Transport across pixels follows the minimal router (P7), implemented in local orthonormal frames of the three-dimensional spatial slice and represented patchwise on the S^2 waist. A global tangent-frame description on S^2 is obstructed, so the screen description is local [26,27]. The induced L_1 step metric approximates the smooth L_2 isotropic limit; the mismatch becomes relevant near the diamond tips where the cross-section becomes sub-resolution, producing an irreducible digitization overhead, parametrized by κ [28].

The interface is the waist S^2. Boundary completion represents interior conserved charge sectors as boundary flux labels (P1, P3, P6), reflecting the Gauss-law requirement that charges in a region be encoded by flux through its boundary. The normalization of the local vector response is therefore tied to the surface geometry. We use the standard infrared convention $\alpha \equiv g^2/4\pi$. In the present boundary formulation, this convention aligns the gauge coupling with the flux normalization through the closed S^2 interface.

1.3. Topological Budget: Effective Internal Degeneracy

The diamond waist S^2 serves as the observer's operational horizon: an instantaneous coherency screen formed by the unique spatial intersection where the past light cone (incoming data from initiation p) meets the future light cone (outgoing responses registered at q). To determine the effective internal degeneracy N of this screen, we define the baseline vacuum capacity functional $S_{\mathrm{vac}} \equiv \sum_i S_i$

from the topological, tip and spin structures specified by P2–P7. This functional counts internal response depth per resolved boundary patch, not the number of patches. The 2π modular periodicity gives this functional its KMS interpretation, while finite resolution makes it a capacity measure for the boundary completion. Physical area enters separately through the number of surface patches (A/L_s^2). Retaining only dimensionless, scale-free terms, S_{vac} separates macroscopic area from internal edge capacity.

Bulk Topology (S_{bulk})

Boundary completion requires a topologically closed interface to satisfy the Gauss-law for interior charge encoding. On the simply connected waist S^2, the available additive, scale-free local curvature integral is the Euler term. We use the scalar-curvature convention, so the Gauss–Bonnet integral gives 8π rather than the Gaussian-curvature value 4π.

The Gauss–Bonnet theorem [29,30] supplies the unique dimensionless closed-waist curvature invariant entering the capacity functional. In the minimal sector, we denote its logarithmic capacity contribution by:

$$S_{\text{bulk}} \equiv \oint_{S^2} R^{(2)}\, dA = 4\pi\chi(S^2) = 8\pi$$

Here S_{bulk} is not a thermodynamic entropy and the Gauss–Bonnet theorem does not by itself count microscopic states. It is a dimensionless logarithmic capacity contribution assigned by the finite-resolution boundary architecture. More generally, one could write $S_{\text{bulk}} = \eta \oint_{S^2} R^{(2)} dA$. The selected minimal sector uses the no-extra-parameter normalization $\eta = 1$, giving $S_{\text{bulk}} = 8\pi$. Choosing $\eta \neq 1$ would introduce an additional boundary-capacity parameter and define a different matching sector.

Finite representatives must preserve this closed topology ($V - E + F = 2$). Open geometries are excluded to avoid unconstrained boundary-circle data.

By Gauss–Bonnet, the waist radius drops out: curvature and area scale inversely, leaving only the Euler invariant. The 8π term is therefore not an area entropy, but the baseline logarithmic capacity weight of the closed gluing surface in the selected normalization. It represents the scale-independent overhead of boundary charge and gluing sectors, analogous to the constant topological contributions familiar from topological entanglement entropy and to the boundary-sector interpretation of edge modes [11,13,31,32]. This structure supports the algebraic gluing required by non-factorization and boundary completion (P1–P3).

A hemisphere is excluded in the selected sector because its boundary circle would require additional edge data and would no longer represent the closed Gauss-law interface used for the capacity functional. Geometric, scale-dependent or multiply bounded choices define different capacity functionals outside the chosen architecture.

The transport input for the capacity budget is the octahedral router ($z = 6$) (P7). A closed modular cycle must treat each local direction and its reverse symmetrically; otherwise the transport layer would introduce directional bias. Tetrahedral coordination ($z = 4$) lacks antipodal pairs and fails inversion symmetry, while an icosahedral router ($z = 12$) adds transport directions beyond those needed to span three dimensions. Within the signed, inversion-symmetric router class, the minimal spanning set $\{\pm x, \pm y, \pm z\}$ fixes $z = 6$ as the minimal transport architecture in the capacity count.

Tip Defect Parameter (κ)

At the diamond tips (p, q), the transverse cross-section falls below the resolution length $L_s \equiv \delta$ (P5). Smooth modular flow can no longer be represented as a continuous transverse field there. It must be recorded as a discrete boundary update on the L_1 transport layer selected by P7.

Physically, the tip is the place where a smooth isotropic flow is forced through a finite, graph-local router. The minimal inversion-symmetric router has three antipodal transport-axis pairs, $\{\pm x, \pm y, \pm z\}$. Since no axis is preferred, one unresolved tip update must be distributed equally over the three independent axes, yielding the spatial factor $1/3$. The same factor appears geometrically in the octahedral Regge construction: a closed triangular transport mesh cannot form a sphere without positive curvature defects. In the octahedral seed graph, four equilateral triangular sectors meet at each pole, so the angular deficit is $2\pi - 4(\pi/3) = 2\pi/3$. The normalized missing angular fraction is therefore $(2\pi/3)/(2\pi) = 1/3$. The six poles sum to 4π, ensuring the sphere curvature closure.

The remaining normalization comes from the intrinsic modular clock; the modular automorphism of the boundary algebra generates a KMS orbit with Euclidean period 2π. Expressing the per-tip defect (impedance) as a leakage rate over one full modular cycle gives:

$$\kappa = \frac{1}{3 \times 2\pi} = \frac{1}{6\pi}.$$

A complete causal-diamond modular cycle crosses both tips p and q, so the cycle-integrated leakage is 2κ. This is not an arbitrary normalization. It is the finite-resolution impedance of the diamond tips: the cost of routing smooth modular flow through a closed, isotropic, discrete boundary graph.

As we will see below, the same tip impedance also controls coherent tensor participation and open-system leakage.

Twist Contribution (S_{twist})

The discrete transport structure (P7) must support local spinors. This requires lifting local rotations from $SO(3)$ to the double cover $SU(2)$. On the boundary algebra, this lift appears as a $\mathbb{Z}_2$ grading that separates bosonic and fermionic transport sectors around closed modular loops.

The contribution counted here is not the Hilbert-space dimension of a local spin-1/2 fiber, which belongs to the matter transport sector. The capacity term instead counts the minimal topological wiring required for the boundary algebra to support the spin-parity holonomy associated with this $\mathbb{Z}_2$ grading. Intuitively, the spinor and the twist count different things. The spinor is the object being transported; the twist is the boundary gluing rule that makes this transport globally consistent.

In the selected minimal non-Abelian edge sector, this wiring is represented by an Ising/Majorana twist defect σ [33], whose fusion rule $\sigma \times \sigma = 1 + \psi$ implies $d_\sigma^2 = 2$ and therefore $d_\sigma = \sqrt{2}$. Physically, two such boundary twists fuse into an ordinary binary fermion-parity channel. A single twist therefore contributes an irreducible half-bit to the logarithmic capacity budget: $S_{\text{twist}} = \ln d_\sigma = \ln \sqrt{2}$.

Choosing $d_\sigma = 2$ would count the local spinor representation rather than the boundary topological twist, thereby double-counting spinorial degrees of freedom already carried by the local matter sector. The $\sqrt{2}$ contribution supplies only the minimal boundary spin-parity grading required to close the finite-resolution algebra; it does not introduce a propagating bulk anyon in $3+1$ dimensions.

In summary, the capacity contribution follows this topological hierarchy:

$$SO(3) \to SU(2) \implies \mathbb{Z}_2 \text{ grading} \implies \text{twist defect} \implies d_\sigma = \sqrt{2} \implies S_{\text{twist}} = \ln \sqrt{2}.$$

Resulting Effective Internal Degeneracy (N)

These three contributions arise from independent requirements: closed algebraic gluing, modular-cycle closure and spinorial lift. In this product configuration, their associated state spaces factorize, so their logarithmic capacities add, yielding the total vacuum capacity per pixel:

$$S_{\text{vac}} = 8\pi + \frac{1}{6\pi} + \ln \sqrt{2}.$$

Because S_{vac} is dimensionless and additive, it has the form of a logarithmic capacity. As in statistical mechanics and holographic entropy, where $S = \ln \Omega$ encodes effective state multiplicity, exponentiation converts this capacity budget into a multiplicative response capacity [16,34,35]. We therefore define the effective channel multiplicity of the selected boundary sector by $N \equiv e^{S_{\rm vac}}$:

$$\boxed{N = \sqrt{2}\,\exp\!\left(8\pi + \frac{1}{6\pi}\right) \approx 1.23 \times 10^{11}}.$$

As an exponentiated effective capacity rather than a microscopic Hilbert-space dimension, N need not be an integer. It quantifies the intensive internal response capacity assigned to each patch on the boundary algebra. Confined strictly to the boundary completion, this multiplicity introduces no additional propagating bulk fields.

1.4. Constitutive Relation (Coherent Participation)

While N is the total internal response capacity, gravitational stiffness samples only the phase-coherent tensor subset that survives one modular cycle. Physically, to participate coherently, a boundary channel must cross the geometric tips without losing its quantum phase. Information that decoheres simply thermalizes into entropy. Only the protected, surviving fraction can sustain macroscopic geometric stress. Let $\Pi_{\rm coh}$ denote the modular-cycle coherent projector on the resolved boundary channel space. We have:

$$\frac{N_{\rm eff}}{N} = \frac{\operatorname{Tr}\Pi_{\rm coh}}{\operatorname{Tr}\mathbf{1}} = \kappa, \qquad N_{\rm eff} \equiv \kappa N.$$

Equivalently, $\operatorname{Tr}\mathbf{1} = N$ and $\operatorname{Tr}\Pi_{\rm coh} = N_{\rm eff}$.

Geometrically, the causal-diamond tips act as the common bottlenecks through which information enters and exits the resolved region. This gives the same finite-resolution defect distinct algebraic roles. In the logarithmic capacity budget, κ contributes additively as a capacity cost. In the tensor response, it contributes multiplicatively as the coherent participation fraction. In both roles, κ is fixed by the modular clock and transport normalization, not tuned to match Newton's constant.

The same tip defect has a third dynamical role. Because a full open-modular cycle crosses both tips, the accumulated leakage is 2κ. As developed in Chapter 2, this leakage manifests as Gorini–Kossakowski–Sudarshan–Lindblad (GKSL) dissipation governed by the Kubo–Mori fluctuation-dissipation response [36–39].

In the linear tensor response, these coherent boundary channels decouple quadratically, allowing their individual stiffnesses to add extensively in the macroscopic Hessian [40,41]. Normalizing each active channel by the fundamental scale M_s^2 yields the macroscopic constitutive relation:

$$M_P^2 = N_{\rm eff} M_s^2.$$

This relation serves as the architecture's sole dimensional calibration. It is not a prediction of Newton's constant: the boundary sector first derives the dimensionless coherent stiffness depth $N_{\rm eff}$, and the observed value of G is then used exactly once to assign physical units to the finite-resolution scale M_s. The construction is strictly non-circular because $N_{\rm eff}$ is fixed internally before G enters.

Within the selected minimal sector, the numerical structure is rigid. The closed-waist capacity weight, the tip defect, the spin-twist sector, the one-tick modular resolution, and the signed three-axis transport architecture fix N and $N_{\rm eff}$. Changing any of these inputs moves the construction to a different boundary sector or matching convention, rather than varying a continuous parameter.

1.5. Numerical Calibration

We now calibrate the resolution scale M_s against Newton's constant G using the reduced Planck mass $M_P = (8\pi G)^{-1/2} \approx 2.435 \times 10^{18}$ GeV throughout to align with the standard Einstein-Hilbert action. With the capacity functional above, $N_{\text{eff}} = \kappa N \simeq 6.51 \times 10^9$. By substituting the constitutive law $M_P^2 = N_{\text{eff}} M_s^2$ and solving for the resolution scale, we obtain:

$$\boxed{M_s = \frac{M_P}{\sqrt{N_{\text{eff}}}} \approx 3.02 \times 10^{13}\,\text{GeV}.}$$

M_s represents the physical resolution limit of the algebra (sharp focus) where the EFT problem is well-posed: gravitational stiffness, gauge couplings and mass gaps enter as matching data, and in quantized sectors some conditions reduce to closed-form constraints (Chapter 3). This calibrated matching scale lies in the intermediate range often associated with high-scale seesaw models and plateau-inflation phenomenology [42,43].

In reduced-Planck units, the inverse stiffness scale is $M_P^{-1} = L_s/\sqrt{N_{\text{eff}}}$. Thus M_s acts as the fundamental resolution limit, while M_P emerges strictly as the collective tensor stiffness of the boundary, eliminating the singular $L_P \to 0$ continuum artifact.

Pixel Saturation Limit

Finite resolution (P5) bounds the local excitation capacity of a single boundary pixel. The internal multiplicity N includes the spin-twist factor $d_\sigma = \sqrt{2}$, which supplies the minimal $\mathbb{Z}_2$ spin-parity grading. Because this edge twist is not an addressable scalar channel, the saturation estimate uses the non-twist channel count $n_{\text{ch}} \equiv N/\sqrt{2}$.

With M_s fixed by the Newton calibration, the single-pixel activation scale is $E_{\text{pix}} \equiv M_s/n_{\text{ch}}$. More generally, a local scalar operator with q fermionic legs is governed by a single-pixel saturation cap $m_{\max}^{(q)} = E_{\text{pix}}/q$. Mass deformations on the boundary-completed algebra must be closed gauge-invariant scalar operators. A hypothetical single-leg insertion ($q = 1$) is therefore inadmissible. Higher-valence scalar operators ($q \geq 4$) further lower the cap, corresponding to higher-dimensional EFT deformations. The leading admissible mass deformation is instead the gauge-invariant bilinear $\bar{\psi}\psi$, fixing $q = 2$:

$$m_{\max}^{(q)} = \frac{E_{\text{pix}}}{q} \xrightarrow{\bar{\psi}\psi,\ q=2} m_{\max}^{(2)} = \frac{E_{\text{pix}}}{2} \approx 174\,\text{GeV}.$$

This resulting upper bound lies close to the observed top-quark mass ($m_t \approx 173$ GeV). This proximity is a heuristic consistency check of the single-pixel saturation cap, not a mass prediction.

Consistency Check: Area Law

We verify that this calibration preserves the Bekenstein–Hawking entropy structure [34,44,45]. For a horizon of area A, the standard entropy (in natural units) is $S_{\text{BH}} = A/4G$. Substituting $1/G = 8\pi M_P^2$ we obtain:

$$S_{\text{BH}} = 2\pi M_P^2 A = 2\pi (N_{\text{eff}} M_s^2) A = 2\pi N_{\text{surf}} N_{\text{eff}},$$

where $N_{\text{surf}} \equiv A/L_s^2 = A M_s^2$ is the number of resolvable boundary pixels on a waist of area A (set purely by geometry); the entropy factors as pixels × effective depth. This horizon entropy is not identical to the logarithmic capacity S_{vac} used to define N. The logarithmic capacity S_{vac} defines the internal channel multiplicity $N = e^{S_{\text{vac}}}$ per resolved patch, while S_{BH} counts the area-extensive entropy generated by the effective tensor-response depth $N_{\text{eff}} = \kappa N$ across all patches.

Converting to bits $(S/\ln 2)$ and taking $A_{\text{cosm}} \sim 4\pi H_0^{-2}$ gives $\sim 10^{122}$ bits. This reproduces the standard Bekenstein–Hawking area law and the familiar cosmic entropy scale, providing a consistency check of the calibration.

The result follows algebraically from the constitutive lock $M_P^2 = N_{\text{eff}} M_s^2$. It shows that the standard horizon entropy can be represented as a resolved pixel count multiplied by an effective tensor-response depth. Channel multiplicity supplies the required information density without shrinking the pixel size to L_P, recovering the Bekenstein–Hawking scaling natively at the finite resolution scale L_s.

Within this framework, M_s is the physical regulator, while the reduced Planck scale is the collective stiffness scale.

1.6. Emergent Time

In a background-independent framework, there is no universal global clock; time must emerge relationally from the system itself [3,46]. Inside any causal diamond, the local quantum state supplies its own intrinsic operational clock τ via modular flow [4,5]. Time is strictly diamond-local: one operational tick corresponds to a single distinguishable boundary update at M_s.

The continuous proper time $t \simeq \delta\tau$ of a macroscopic observer emerges only after coarse-graining these updates. With the local clock and boundary algebra fixed, diamond dynamics reduces to statistical inference on constant operator content [47,48]. This variational problem matches a finite boundary record to a reference state, rather than evolving in external time. Physical time evolution enters when the resolved workspace shifts from one causal diamond to the next.

This entropic view of quantum evolution directly motivates the relative-entropy variational principle developed in Chapter 2.

2. Relative-Entropy Functional and Dynamics

Dynamics on a causal diamond emerge not as the time-evolution of a global Wheeler–DeWitt state [1], but as local statistical inference. In algebraic quantum field theory (AQFT), infinite local degrees of freedom (Type III algebras) break standard density matrices and traces. We restore mathematical rigor by evaluating them at finite resolution on the boundary-completed effective algebra $\mathfrak{A}_O$, where the reference KMS state is faithful [18,49]. On this shared algebra, the reduced boundary state ρ_O supplies the local data, while geometry and other background fields enter exclusively through a semiclassical reference family $\sigma_O[\Lambda]$. The resolved algebra defines the operational arena: it fixes which physical distinctions the causal diamond can actually register.

While standard entanglement-equilibrium methods rely on continuum locality [6–8,50–55], this framework anchors the subsystem at finite resolution on a boundary-completed algebra, transforming the variational problem into a matching-scale effective theory at $M_s = \delta^{-1}$ [56]. The local dynamics are organized by the relative entropic mismatch functional $I[\Lambda; O] = S_{\rm rel}(\rho_O \| \sigma_O[\Lambda])$ at fixed $(O, \mathfrak{A}_O, \delta)$ [47,49,57]. Relative entropy therefore measures the information cost of explaining the fixed boundary data with a deformed background Λ. Around a matched reference point, its Hessian naturally decouples into independent tensor, vector and scalar blocks, making a joint matching of all three sectors well-posed.

We keep four layers separate: the axioms P1–P7, the calibrations of Chapter 1, the selected minimal implementation and the EFT matching approximations.

We use N for total internal channel multiplicity per pixel (boundary patch), $N_{\rm eff} = \kappa N$ for effective coherent participation, κ for the tip impedance factor, $k \in \mathbb{Z}$ for the WZW level, α for the gauge coupling and M_s for the resolution scale.

2.1. Entropic Variational Principle and Operational Domain

We fix the container $(O, \mathfrak{A}_O, \delta)$ with proper-distance regulator $\delta = M_s^{-1}$ ($\delta \ll \ell_O \ll R_{\rm curv}$), varying only the reference family $\sigma_O[\Lambda]$ on the fixed algebra $\mathfrak{A}_O$. We define the variational functional [57]:

$$I[\Lambda; O] \;:=\; S_{\rm rel}(\rho_O \,\|\, \sigma_O[\Lambda]).$$

Boundary completion (P3) supplies the common operator domain on which $S_{\rm rel} \geq 0$ is well defined and monotone under further restriction [18,49,57,58]. On this fixed algebra, we adopt an exponential reference family as the maximum-entropy formulation compatible with the chosen sources Λ [47,49]:

$$\sigma_O[\Lambda] = \frac{e^{-K_O[\Lambda]}}{\mathrm{Tr}(e^{-K_O[\Lambda]})}.$$

The modular generator $K_O[\Lambda]$ couples the local background multiplet Λ to the boundary operator multiplet $\mathcal{O}$, defining deformations via the inner product:

$$\delta K = \int d^4x\,\sqrt{-g}\,\delta\Lambda(x)\cdot\mathcal{O}(x).$$

This integral serves as the quasi-local continuum shorthand for boundary-smeared operators after modular averaging. In the KMS regime, relative entropy takes the modular free-energy form [57]. At the matched point $\rho_O = \sigma_O[\Lambda_0]$, reference variations are tangent to a normalized exponential family. The linear relative-entropy term vanishes, reflecting the local entanglement first law [57,59,60]:

$$S_{\rm rel}(\rho\|\sigma) = \Delta\langle K_\sigma\rangle - \Delta S \quad (K_\sigma = -\log\sigma), \qquad \delta I\big|_{\Lambda_0} = 0.$$

With the linear term absent, the restoring response in the local stationary expansion is strictly quadratic, governed by the Hessian.

We vary the reference background $g \mapsto \sigma_O[g]$ at fixed $(O, \mathfrak{A}_O, \delta)$. Metric variations deform $K_O[g]$ and the correlators on the same boundary-completed algebra; they do not move the endpoints (p,q) or the regulator. The regulator remains at fixed proper distance $\delta = M_s^{-1}$ from the waist, so the unresolved tip region stays in the Chapter 1 operational class and imports the tip parameter κ.

2.2. Hessian Bridge, Spectral Representation and EFT Coefficients

Local background fields (metric $g_{\mu\nu}$, gauge field A_μ, scalar φ) couple on the boundary algebra to three composite operators: the stress tensor $T^{\mu\nu}$, the conserved current J^μ, and the scalar density M. Within the finite-resolution boundary-completed algebra $\mathfrak{A}_O$, the leading Hessian kernel $G_{IJ}(x,y)$ block-diagonalizes across these source sectors at the symmetric matched KMS reference. This separation follows from the source labels preserved by the boundary architecture.

Modular flow, generated by the geometric boost $K_{\rm mod}$ (P4), is fixed by the causal diamond and its waist. The source-label symmetries retained by the boundary-completion architecture commute with the reference modular flow, $[K_{\rm mod}, Q] = 0$ [11,61]. Metric, gauge-connection, and scalar deformations therefore transform as inequivalent source modules. Any nonzero mixed Hessian block must define a symmetry-preserving map between inequivalent source modules.

Schur's lemma, together with Ward identities, forces such maps to vanish in the leading quadratic response: $G_{IJ}(x,y) = 0$ for $I \neq J$.

The discrete L_1 router (P7) contributes only subleading anisotropic corrections, assigned to the $O(M_s^{-2})$ EFT remainder, and these average to zero over the modular period 2π under the octahedral projection. The $\mathbb{Z}_2$ twist acts as a topological superselection rule, partitioning the algebra into bosonic and fermionic sectors whose center is preserved by modular flow. At the symmetric reference, no mixed correlators survive the KMS-weighted projection at leading order. To fix normalizations unambiguously, the source–operator pairing is

$$\delta K = \int d^4x\sqrt{-g}\left(\frac{1}{2}\,\delta g_{\mu\nu}\,T^{\mu\nu} + \delta A_\mu\,J^\mu + \delta\varphi\,M\right),$$

where the factor $1/2$ is the usual metric-source convention.

These sources probe three distinct mismatches: geometric stress, charge transport and local occupancy. Expanding around the reference KMS state Λ_0 gives the standard variational series:

$$I[\Lambda_0 + \delta\Lambda] = I[\Lambda_0] + \int d^4x\,\delta\Lambda(x)\cdot\frac{\delta I}{\delta\Lambda(x)}\bigg|_{\Lambda_0} + \frac{1}{2}\iint d^4x\,d^4y\,\delta\Lambda(x)\cdot\underbrace{\frac{\delta^2 I}{\delta\Lambda(x)\delta\Lambda(y)}\bigg|_{\Lambda_0}}_{G(x,y)}\cdot\delta\Lambda(y) + \mathcal{O}(\|\delta\Lambda\|^3)$$

At equilibrium, $\rho_O = \sigma_0$, so $I[\Lambda_0]$ and the first variation vanish. The leading response is therefore quadratic and governed by the Hessian kernel:

$$G(x,y) := \left.\frac{\delta^2 I}{\delta\Lambda(x)\delta\Lambda(y)}\right|_{\Lambda_0}.$$

Centering tangent modular operators, the Hessian becomes the connected Kubo–Mori correlator, the KMS-weighted two-point response at the matched reference state (P4) [38,39,57]:

$$\langle \delta K|\delta K\rangle_\sigma = \int_0^1 ds\ \mathrm{Tr}\big(\sigma^s \delta K\, \sigma^{1-s}\delta K\big).$$

The quadratic contribution to I is therefore $\frac{1}{2}\langle \delta K|\delta K\rangle_{\mathrm{KM}}$ near the matched KMS state. The Hessian is the local stiffness matrix of distinguishability [59].

Because modular flow acts as a geometric boost (P4) and transport-layer anisotropy averages to zero over a full 2π orbit, the reference vacuum is isotropic and parity-even. Local deformations therefore decompose into orthogonal spin channels (transverse-traceless tensors, conserved vectors, scalars), with the $\mathbb{Z}_2$ grading (P7) isolating the fermionic sector. By symmetry, Kubo–Mori cross-pairings between these representations vanish:

$$\langle \delta g|\delta A\rangle_{\mathrm{KM}} = \langle \delta g|\delta\varphi\rangle_{\mathrm{KM}} = \langle \delta A|\delta\varphi\rangle_{\mathrm{KM}} = 0.$$

This block decomposition applies to the leading quadratic Kubo-Mori response at the symmetric matched KMS reference state. It is a tangent-space statement. It does not exclude higher-order or nonlinear mixed interactions. KMS compatibility alone is not sufficient for an operator to enter the leading Hessian. The operator must also satisfy the full source-label constraints: gauge invariance, index contraction, Ward identities, parity, isotropy and modular labels.

The Hessian therefore block-diagonalizes at leading order (mixed terms either vanish under projection or enter at higher order).

This theoretical block-diagonalization is verified computationally in the supplementary toolbox `hessian_sector_decoupling.py` [62]. The simulation builds an octahedrally refined finite S^2 boundary, starts from a generic dense local fiber Hessian with tensor/vector/scalar mixing, and then applies the finite octahedral Reynolds projection. The projected heatmap in Figure 1 shows the resulting trace-free tensor, vector and scalar response blocks. The dense pre-projection matrix and the contamination controls are provided in the supplementary dashboard.

KMS compatibility alone does not place a mixed-gradient operator in the leading tangent Hessian. Terms such as $F_{\mu\nu}\partial^\mu\phi$ and $T^{\mu\nu}\partial_\mu\phi\,\partial_\nu\phi$ either require scalar completion, vanish at the homogeneous matched reference where $\partial_\mu\phi = 0$, or reduce to total derivatives on the closed $S^3\times S^1$ history manifold. Any remaining mixed-gradient contributions belong to the M_s^{-2}-suppressed EFT remainder and do not affect the leading tensor/vector/scalar matching.

Low-momentum sources ($|p| \ll M_s$) effectively commute with the modular background. This kinematic suppression reduces the Kubo–Mori kernel to its leading gradient expansion, yielding a symmetric spectral trace over the covariant transport operator fixed by P7:

$$\langle \delta K|\delta K\rangle_{\mathrm{KM}} \approx \mathrm{Tr}\Big(\delta K\, f(D_{\mathcal{A}}^2/M_s^2)\,\delta K\Big),$$

where the positive modular window $f(\tau)$ is obtained by integrating the KMS kernel over the resolved modular interval $[\varepsilon, 2\pi-\varepsilon]$ with $\varepsilon = 1$.

The same finite resolution $M_s \equiv \delta^{-1}$ that defines the stretched horizon also sets the physical EFT cutoff (Nyquist frequency). Deformations with physical momentum $|p| > M_s$ are unresolved and integrated out of the effective description (effectively aliased away). Evaluated on the $S^3\times S^1$ history manifold, the heat-kernel trace extracts the local EFT coefficients. This spectral operation

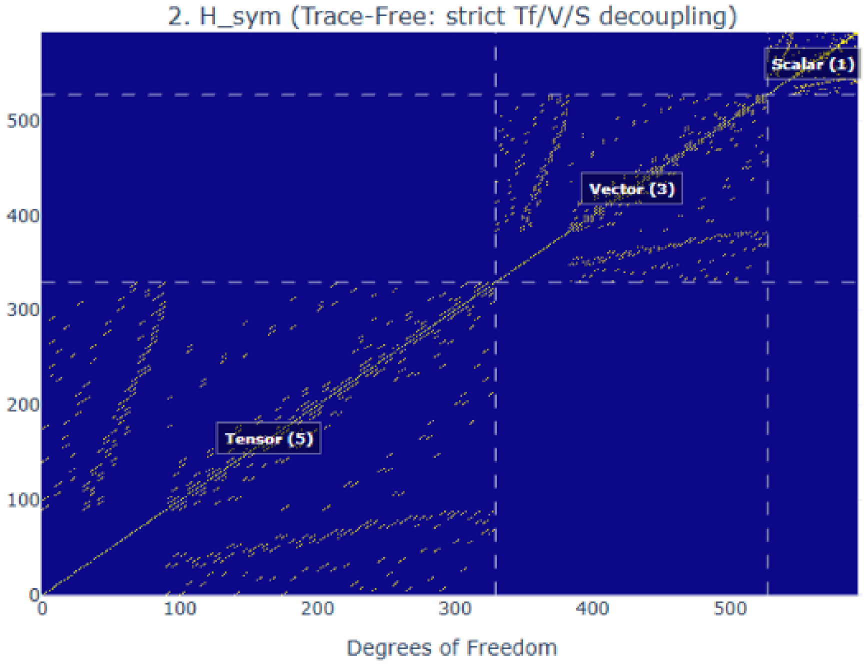

Figure 1. Symmetry-projected finite-boundary Hessian. The octahedral projection separates the trace-free tensor, vector and scalar source modules into orthogonal response blocks; off-block entries vanish to numerical precision. Computed via [62].

isolates the numerical prefactors while preserving the physical source insertions. Operationally, the heat kernel counts the resolved modes available to carry each response and packages them into local EFT coefficients.

Expressing the window f via Laplace transform, we insert the short-time heat-kernel expansion $\mathrm{Tr}\, e^{-tD^2} \sim \sum_n a_n t^{(n-4)/2}$ [63,64]. With irrelevant corrections constrained by the Monotone Spectral Suppression corollary (P5), this yields finite EFT coefficients a_n:

$$\mathrm{Tr}\, f(D_{\mathcal{A}}^2/M_s^2) \sim \sum_n a_n \left(\int_0^\infty dt\, t^{(n-4)/2} \tilde{f}(t) \right) M_s^{4-n}.$$

Note that the standard Seeley–DeWitt coefficients encode the local geometric invariants ($a_2 \propto R$ and $a_4 \propto R^2, F^2$).

At low derivative order, locality and symmetry fix the operator basis, mapping the independent Hessian blocks directly to the physical effective action:

$$\delta^2 I \simeq \underbrace{\frac{1}{2} \iint \delta g_{\mu\nu}\, G_{TT}\, \delta g_{\rho\sigma}}_{\Rightarrow \int d^4x \sqrt{-g}\, \frac{M_P^2}{2} R} + \underbrace{\frac{1}{2} \iint \delta A_\mu\, G_{JJ}\, \delta A_\nu}_{\Rightarrow \int d^4x \sqrt{-g}\, \frac{1}{4g^2} F^2} + \underbrace{\frac{1}{2} \iint \delta\varphi\, G_{MM}\, \delta\varphi}_{\Rightarrow \int d^4x \sqrt{-g}\, \mathcal{L}_{\mathrm{mass}}} .$$

To isolate the resulting dynamic restoring forces, we absorb all static vacuum-energy contributions directly into the reference state.

At leading two-derivative order, the tensor block directly matches the Einstein–Hilbert coefficient. We extract these local EFT parameters by evaluating the heat-kernel trace over the modular manifold $S^3 \times S^1$ at the finite bandwidth M_s. Below this threshold, standard renormalization group running takes over. Consequently, the cutoff M_s is not an ad hoc external regulator [65,66], but the physical threshold where the boundary algebra stops distinguishing finer structure.

2.3. Coupling Factorization and Spectral–Volume Correspondence

Quasi-locality factorizes the leading quadratic response of slowly varying fields into an effective four-volume, an intensive coupling and a local average. Absorbing the universal density-of-states factors yields [63,64]:

$$\mathrm{Tr}_{\mathcal{D}}\mathbf{1}_{\mathfrak{A}} \simeq NM_s^4\mathrm{Vol}_4(\mathcal{D}) \quad \Longrightarrow \quad \mathrm{Vol}_4(\mathcal{D}) = \frac{\mathrm{Tr}_{\mathcal{D}}\mathbf{1}_{\mathfrak{A}}}{NM_s^4}$$

This acts as a finite-resolution analogue of Weyl's law. The spectral trace counts the total resolved states; dividing it by NM_s^4 factors out the microscopic capacity. This strips away the sub-resolution details, leaving only the coarse-grained four-volume seen by the infrared EFT.

Here, N counts the available internal response channels. The effective volume is inferred from the spectral mode count rather than assumed as a primitive coordinate measure. The tensor sector samples the coherently participating subset $N_{\mathrm{eff}} = \kappa N$, making Einstein stiffness extensive in channel number. By contrast, the vector and scalar sectors are normalized per channel, so the gauge stiffness $1/g^2$ and mass susceptibilities remain intensive responses at M_s.

The spectral trace over the minimal compact operational history then establishes a spectral–volume correspondence. In the small-diamond/KMS regime modular time forms a thermal circle S^1 [4,18]. Identifying the spatial part as two B^3 halves glued across the waist ($B^3 \cup_{S^2} B^3 \simeq S^3$), the minimal manifold for the trace is $S^3 \times S^1$ [63].

This correspondence converts the spectral trace into an effective four-volume at resolution M_s. Separating the state count from the volume cleanly isolates the scaling: tensor stiffness grows extensively with the coherent channels, while charge and scalar susceptibilities remain intensive.

2.4. Tensor Sector: Gravity as Extensive Stiffness

Applying the Hessian mapping to $\delta g_{\mu\nu}$, the tensor block G_{TT} measures the stiffness of the geometric pixel under modular flow. In the low-curvature regime $|R| \ll M_s^2$, linear response around the modular vacuum governs the dynamics [6]. In the small-diamond KMS regime, the modular generator couples $\delta g_{\mu\nu}$ to the stress tensor $T^{\mu\nu}$ (via the conformal Killing vector), supplemented by the boundary completion term required on bounded regions. Its variation reproduces the geometric entropy functional of the cut (area/Wald-type) [4,11,16,34].

With the first variation vanishing at equilibrium, the second variation governs the tensor response. At low curvatures, locality, parity and diffeomorphism invariance restrict this leading two-derivative response to the Einstein–Hilbert invariant [7,10,60,67,68]. Absorbing the identity contribution into the reference state isolates gravitational stiffness from the vacuum-energy prescription. The absolute coefficient for this emergent tensor structure is then assigned using the macroscopic Newton calibration ($M_P^2 = N_{\mathrm{eff}}M_s^2$) imported from Chapter 1. Gravity is extensive because coherent boundary channels resist geometric deformation collectively.

2.5. Vector Sector: Gauge as Intrinsic Susceptibility

Applying the Hessian mapping to δA_μ, the vector block G_{JJ} measures the intrinsic susceptibility of the boundary current, specifically the linear response of the boundary state to an external connection. A weak background connection couples to the conserved edge current J^μ, required by the CS/WZW structure [21,24], through the modular generator:

$$\delta K[A] = \int d^4x\sqrt{-g}\, A_\mu(x)\, J^\mu(x).$$

Ward identities enforce gauge invariance, restricting this vector response to the field strength tensor. Because the reference state is parity-even, the matching isolates the standard kinetic term ($F_{\mu\nu}F^{\mu\nu}$), leaving parity-odd topological terms unconstrained. Gauge susceptibility emerges as a geometric property determined by the fluctuation-dissipation relation of the boundary algebra [38,39].

By P5 corollary, finite resolution truncates the operational modular interval to $\tau \in [1, 2\pi - 1]$. On the 1D modular orbits, the angularly averaged chiral current takes the standard affine level form $\langle J(\tau)J(0)\rangle = \frac{k}{4}\sin^{-2}(\tau/2)$ [69]. The level $k \in \mathbb{Z}$ is defined in the trace convention fixed by the boundary current normalization.

Let ϵ be a formal symmetric endpoint for the modular window. The raw modular current fluctuation is:

$$\chi_{\rm pix}(\epsilon) = \frac{k}{4}\int_{\epsilon}^{2\pi-\epsilon} \csc^2(\tau/2)\, d\tau = k\cot(\epsilon/2).$$

With a sensitivity of $d\ln\chi_{\rm pix}/d\epsilon = -1/\sin\epsilon$, this raw fluctuation clearly depends on the chosen window. However, this dependence is purely kinematic and universal across all current sectors. Factoring out the common modular-window factor, $I_{\rm mod}(\epsilon) = 4\cot(\epsilon/2)$, isolates the physical susceptibility:

$$\bar{\chi}_{\rm pix}(\epsilon) = \frac{\chi_{\rm pix}(\epsilon)}{I_{\rm mod}(\epsilon)} = \frac{k}{4}.$$

The endpoint dependence cancels exactly, leaving only the integer current level k. All group-theory factors and trace normalizations are absorbed into this k.

The canonical choice $\epsilon = 1$ represents one minimal modular update on the discrete boundary algebra. It fixes the readout convention at the matching scale M_s; it is not a continuously sliding Wilsonian cutoff. Standard renormalization-group running applies only below M_s.

Physically, ϵ merely scales the kinematic readout, while the true gauge stiffness is fixed by the normalized topological response. Applying the volume-coupling factorization to match this quadratic response to the canonical gauge term $-\frac{1}{4g^2}F^2$ identifies the inverse coupling $1/g^2 = 4\bar{\chi}_{\rm pix} = k$. Utilizing the standard flux convention $\alpha \equiv g^2/4\pi$, this yields the matching-scale inverse coupling:

$$\frac{1}{g^2} = 4\bar{\chi}_{\rm pix} = k \qquad \Longrightarrow \qquad \alpha^{-1}(M_s) = 4\pi k.$$

This matching applies to each normalized current block, with Abelian factors requiring a fixed charge convention. Thus, $\alpha^{-1}(M_s) = 4\pi k$ is a rigidly quantized boundary condition, not a continuum cutoff artifact. The continuous low-energy gauge couplings are then obtained by standard renormalization-group evolution from these discrete topological boundary data.

The same vector-sector relative-entropy Hessian also defines a distinct infrared observable: the static transverse electromagnetic susceptibility, with pure-gauge zero modes removed. Varying the relative entropy against a physical zero-frequency source over $S^3 \times S^1$ schematically defines the on-shell static response, $\alpha^{-1}(0) \equiv \delta^2 S_{\rm rel}/\delta A^2|_{\omega=0}$, as the fully coarse-grained susceptibility of the boundary-completed current block. Thus, $\alpha^{-1}(M_s)$ and $\alpha^{-1}(0)$ are two projections of the same Kubo–Mori response: the first is the resolved matching condition at the finite-resolution scale, while the second is the macroscopic thermodynamic response.

2.6. Scalar Sector: Mass as Occupancy Stiffness

Applying the Hessian mapping to $\delta\varphi$, the scalar block G_{MM} measures the susceptibility of the selected scalar density; for fermions, the minimal gauge-invariant density is $M = \bar{\psi}\psi$. We couple the source φ to this selected operator via:

$$\delta K_M = \int d^4x\sqrt{-g}\;\delta\varphi(x)\,\bar{\psi}(x)\psi(x).$$

In the symmetry decomposition, $\bar{\psi}\psi$ is a Lorentz scalar, so mass resides in this block. The scalar response identifies the mass operator as the leading relevant deformation, serving as a matching prescription (rather than an independent spectrum derivation):

$$S_{\rm mass} \approx -\int d^4x\sqrt{-g}\; m\,\bar{\psi}\psi.$$

Mass therefore emerges as the energetic cost of maintaining a local fermion occupancy. The $\mathbb{Z}_2$ grading (P7) admits spinor representations [70], whose discrete transport reduces locally to the Dirac operator:

$$D_\mu = \partial_\mu + \frac{1}{4}\omega_\mu^{ab}\gamma_{ab} - iA_\mu^a T^a.$$

Independent of finite capacity, fermionic statistics enforce binary occupancy $n \in \{0,1\}$. In discrete modular time, a local mass gap acts as the on-site phase accumulated per update. Parameterizing $\theta_f \simeq m_f/E_{\text{pix}}$ (subject to $|\theta_f| \le \pi$) and using the per-pixel energy budget E_{pix} from Chapter 1 gives the heuristic scaling rule $m \propto m_{\text{anchor}}/\Omega_{\text{int}}$, where Ω_{int} counts the resolved internal modes accessible at M_s [63,64].

2.7. Unified Matching-Scale Action at M_s

The operators derived above govern the low-curvature regime. To model finite-resolution saturation, we restrict the matching to the reduced homogeneous scalar-curvature sector. In this sector, the only retained local four-derivative invariant is R^2; the Gauss–Bonnet density is topological and anisotropic curvature structures are not retained.

Finite resolution (P5) supplies the sole intrinsic scale M_s, so the saturation completion takes the form $(M_P^2/2)R + \lambda R^2$. Extracting λ therefore reduces to comparing the R and R^2 coefficients within a single scalar heat-kernel expansion. The R^2 term supplies the saturation correction to Einstein stiffness. Finite capacity (P5) together with the isotropic, inversion-symmetric transport layer (P7) selects the conformal Laplacian as the massless scalar transport operator in the minimal bosonic implementation:

$$\Delta_c = -\nabla^2 + E, \qquad E = R/6.$$

This conformal choice (P7) eliminates the arbitrary curvature coupling ξ of a generic scalar operator $-\nabla^2 + \xi R$, isolating the gravitational scalar sector while leaving the spinorial lift of matter to separate fermionic blocks. On the closed $S^3 \times S^1$ history manifold, total derivatives vanish and $\Omega_{\mu\nu} = 0$. The matching applies identical modular-moment normalization to the retained curvature terms, defining the selected spectral protocol.

The relevant Seeley–DeWitt coefficients then reduce to local curvature integrals. The two-derivative term is $a_2 = (4\pi)^{-2}\int d^4x\,\sqrt{g}\,(R/3)$. On $S^3 \times S^1$, curvature resides entirely on the constant-curvature S^3 factor, while the S^1 factor is flat. Hence $R_{\mu\nu}R^{\mu\nu} = R_{\mu\nu\rho\sigma}R^{\mu\nu\rho\sigma} = R^2/3$. Substituting these identities and $E = R/6$ into the standard four-dimensional a_4 coefficient [63] cancels the Ricci-squared and Riemann-squared terms, collapsing the surviving scalar polynomial to:

$$a_4 = (4\pi)^{-2}\int d^4x\,\sqrt{g}\,\frac{R^2}{18}.$$

This directly isolates the scalar-curvature projection of the spectral response. The reduced local curvature coefficients are $c_R = 1/3$ and $c_{R^2} = 1/18$, so $c_{R^2}/c_R = 1/6$. Matching the R term to the Einstein–Hilbert normalization $(M_P^2/2)R$ and accounting for the relative mass dimension M_s^{-2} gives:

$$\lambda = \frac{M_P^2}{2}\left(\frac{1}{6M_s^2}\right) = \frac{M_P^2}{12M_s^2} = \frac{N_{\text{eff}}}{12} \approx 5.42 \times 10^8.$$

Below the matching scale M_s, Wilsonian decoupling confines finite-resolution corrections to higher-derivative operators. At infrared scales $E \ll M_s$, the locked coefficient receives a relative correction of order $\mathcal{O}(E^2/M_s^2)$. These subleading effects enter through the suppressed EFT remainder, preserving the plateau coefficient as a fixed matching-scale boundary condition without introducing a new free parameter.

Within this reduced homogeneous sector, the operational inputs of finite capacity and isotropic transport have a calculable EFT consequence: the heat-kernel trace fixes the R^2 saturation coefficient λ

Preprints.org (www.preprints.org) | NOT PEER-REVIEWED | Posted: 22 May 2026 doi:10.20944/preprints202601.1205.v5

by the ratio M_P^2/M_s^2. This large parameter reflects the hierarchy between the collective stiffness scale M_P and the fundamental scale M_s, yielding $M_R = M_s$ and placing the high-curvature completion in the Starobinsky/plateau class [43,71].

At the matching scale, the local action is the EFT representative whose second variation reproduces the block-diagonal Kubo-Mori Hessian. Because the response sectors are strictly orthogonal at the symmetric matched KMS reference, the unified action contains no leading mixed interactions. Ward identities and derivative counting map the tensor, vector and scalar/spinorial response blocks to $R + R^2$, $F_{\mu\nu}F^{\mu\nu}$ and the Dirac kinetic plus mass-deformation terms. The resulting matching-scale action is:

$$\mathcal{L} = \underbrace{\frac{M_P^2}{2}R + \frac{M_P^2}{12M_s^2}R^2}_{\substack{\text{Einstein stiffness + } R^2 \text{ plateau} \\ \text{tensor sector, extensive in } N_{\text{eff}}}} - \underbrace{\frac{1}{4g(M_s)^2}F_{\mu\nu}F^{\mu\nu}}_{\substack{\text{Yang–Mills kinetic} \\ \alpha^{-1}(M_s)=4\pi k\text{, vector sector}}} + \underbrace{\bar{\psi}i\gamma^\mu D_\mu\psi - m\bar{\psi}\psi}_{\substack{\text{Dirac kinetic + mass} \\ \text{spinorial/scalar sector}}} + \cdots .$$

Here, $F_{\mu\nu}$ is the Yang–Mills field strength, ψ the Dirac fermion and D_μ the gauge- and spin-covariant derivative. The tensor sector yields the emergent Einstein-Hilbert structure (whose absolute scale is anchored by the macroscopic M_P calibration) and, within the reduced homogeneous curvature sector, fixes its dimensionless R^2 plateau completion. The vector sector contributes the Yang-Mills kinetic term with $\alpha^{-1}(M_s) = 4\pi k$, the spinorial transport block supplies the Dirac kinetic term and the scalar block contributes the leading mass deformation. Within this selected sector, no additional continuous coefficient is introduced in the matching step beyond the implementation choices and Chapter 1 constitutive calibration.

This Lagrangian does not quantize gravity; instead, it matches the leading gravitational, gauge and matter sectors as orthogonal projections of the relative-entropy quadratic response on $\mathfrak{A}_O$ at the matching scale, where the discrete update layer admits a continuum field description. The extracted coefficients therefore characterize the observation layer (the lens) rather than the underlying microscopic object, encoding above-cutoff responses into fixed parameters and preventing them from being reintegrated in the low-energy effective theory. Below this cutoff, standard EFT renormalization applies.

2.8. Relation to Continuum Approaches

This formulation reorganizes standard quantum-gravity logic around finite-resolution local inference, complementing continuum entropic programs [6,8,52,72,73] by explicitly enforcing background independence and finite resolution. Rather than deriving classical spacetime from a microscopic path integral, gravitational, gauge, and matter sectors emerge jointly as the structured response of the boundary-completed finite-resolution algebra. Within the causal diamond $(\mathcal{O}, \mathfrak{A}_O, \delta)$, non-factorization (P1) forces boundary completion, while finite resolution (P5) supplies the physical bandwidth $M_s = \delta^{-1}$. This renders the inference problem well-posed: the states ρ_O and $\sigma_O[\Lambda]$ share identical operator content, confining all response to a finite physical scale rather than a formal continuum limit.

The relative-entropy Hessian (Kubo–Mori metric [38]) governs the leading near-equilibrium response on the resolved algebra, allowing the algebraically isolated tensor block to match the Einstein–Hilbert action as the lowest-order two-derivative invariant. By representing this Kubo–Mori response as a spectral trace, this framework also physically motivates the spectral-action principles of noncommutative geometry [65,66]. Rather than imposing the spectral trace as a top-down geometric postulate, it is used here as the effective matching construction for the modular Hamiltonian at the operational scale M_s.

This operational threshold defines the bandwidth below which continuum EFT and standard renormalization-group flows apply. It anchors entropic and spectral approaches to finite informational capacity. Phenomenological modified-spacetime models often introduce $f(R)$ backgrounds or GUP-corrected tunnelling parameters to study finite-length and higher-curvature effects in black-hole thermodynamics [74,75]. The present construction is complementary but more constrained: the finite bandwidth M_s and the reduced R^2 coefficient are fixed by boundary relative-entropy matching, rather than introduced as external $f(R)$ or GUP parameters.

2.9. Time Evolution as Open Modular Dynamics and Walsh Filtration

The Hessian governs restoring forces inside a fixed diamond. Physical time evolution requires shifting the local causal workspace to the next causal diamond. Finite resolution (P5) pushes the causal-diamond tips below the regulator scale δ. Because the Hilbert space does not factorize (P1), the resolved description is expressed instead as an inclusion of accessible algebras, $\mathfrak{A}_{\text{res}} \subset \mathfrak{A}_{\text{full}}$.

Passing from one resolved diamond to the next coarse-grains over sub-resolution data. We model this update (in the Schrödinger picture) by a completely positive trace-preserving (CPTP) map [17,76] that tracks only shared observables, rendering the evolution of resolved states effectively non-unitary. In the Markovian limit, these updates approach a time-homogeneous GKSL semigroup:

$$\frac{d\rho}{d\tau} = -i[H_{\text{eff}}, \rho] + \sum_{a,\omega} \gamma_a(\omega) \left(L_{a,\omega} \rho L_{a,\omega}^{\dagger} - \frac{1}{2} \{ L_{a,\omega}^{\dagger} L_{a,\omega}, \rho \} \right),$$

where the proper time of an external observer scales as $t \simeq \delta\tau$ [36,37].

Finite resolution makes the diamond-to-diamond update intrinsically open. Shifting the observational window coarse-grains data exiting the resolved boundary, especially near the sub-resolution tips. Because the resolved state can remain correlated with inaccessible degrees of freedom, the local update must be a completely positive trace-preserving map,

$$\Phi(\rho) = \sum_a K_a \rho K_a^{\dagger}, \qquad \sum_a K_a^{\dagger} K_a = I.$$

Local irreversibility is therefore an operational consequence of finite-resolution inference, not a violation of global Wheeler–DeWitt stationarity.

Dissipation is not introduced as an independent scale. The same Kubo–Mori kernel that governs the Hessian also sets the coarse-grained leakage, with its dimensionless coefficient fixed by the tip parameter κ [38,39]. A single finite-resolution bottleneck therefore controls both tensor stiffness and open-modular irreversibility.

A generic CPTP map does not by itself select this generation structure. The mechanism used here is more specific: graph transport on the finite boundary combined with localized pole aliasing at the six octahedral defects. This update preserves the invariant sector while damping non-invariant boundary data.

The operational update can be summarized by the axiomatic chain

$$(P1, P3, P5) \Rightarrow \rho_{\text{res}} \xrightarrow{\text{CPTP}} \mathcal{E}_\tau = e^{\tau\mathcal{L}} \xrightarrow{\text{Markov/GKSL}} \mathfrak{A}_{\text{eff}} = \text{Fix}(\mathcal{E}_\tau) \xrightarrow{\text{dephase}} G \to \mathfrak{g} \to T.$$

This chain describes the loss of accessible symmetry data under finite-resolution updating. It is retained as the coarse open-modular filtration of symmetry information. It is no longer used as a stage-counting argument for generations.

The generation-relevant structure comes from the signed boundary transport algebra. The signed octahedral transport layer carries three independent orientation signs, forming $\Gamma \simeq (\mathbb{Z}_2)^3$. The natural Fourier transform on this binary space is the Walsh transform. It decomposes the eight orientation modes into invariant, single-axis, two-axis and three-axis sectors, $\mathbb{C}[\Gamma] = \mathcal{W}_0 \oplus \mathcal{W}_1 \oplus \mathcal{W}_2 \oplus \mathcal{W}_3$, with dimensions $(1, 3, 3, 1)$.

The invariant sector $\mathcal{W}_0$ is the fixed sector. The generation carrier is the degree-one tangent module,

$$\mathcal{F}_3 \equiv \mathcal{W}_1 = \text{span}\{\chi_x, \chi_y, \chi_z\}, \qquad \dim \mathcal{F}_3 = 3.$$

This is the algebraic origin of the "three". It is not the number of stages in $G \to \mathfrak{g} \to T$; it is the dimension of the elementary tangent module selected by the signed boundary transport algebra.

The two-axis sector $\mathcal{W}_2$ also has dimension three, but it represents composite two-axis data such as xy, xz and yz. It is therefore grouped with the higher multi-axis sector $\mathcal{W}_{\geq 2} \equiv \mathcal{W}_2 \oplus \mathcal{W}_3$, giving the diagnostic filtration $1 + 3 + 4 = 8$. The open update thus separates one fixed sector, three elementary tangent modes and four higher multi-axis modes.

Walsh sectors are distinguished dynamically by their Hamming degree m, the number of active transport axes. In the symmetric pole-aliasing channel, degree-m modes have eigenvalues $\lambda_m = \mu^m$ ($0 < \mu < 1$). This establishes a strict spectral gap $\Delta_{12} = \lambda_1 - \lambda_2 = \mu(1-\mu) > 0$ between the degree-one tangent sector $\mathcal{W}_1$ and the degree-two composite sector $\mathcal{W}_2$. The invariant sector $\mathcal{W}_0$ remains fixed, making $\mathcal{W}_1$ the least-damped non-invariant tangent sector. Conversely, the composite sector $\mathcal{W}_2$ joins the damped multi-axis modes, an ordering confirmed by the finite-mesh diagnostic [62]. The generation-carrier is therefore selected as the leading non-invariant Walsh sector.

The supplementary script `open_modular_lie_filtration.py` [62] provides a finite computational verification of this Walsh filtration. It builds an octahedrally refined S^2 boundary mesh, evolves 8×8 orientation states under graph transport with localized pole aliasing and projects the resulting finite update into the Walsh basis.

Figure 2 shows the resulting diagnostic cube. It is not a hand-drawn classification, but a visualization extracted from the simulated CPTP update.

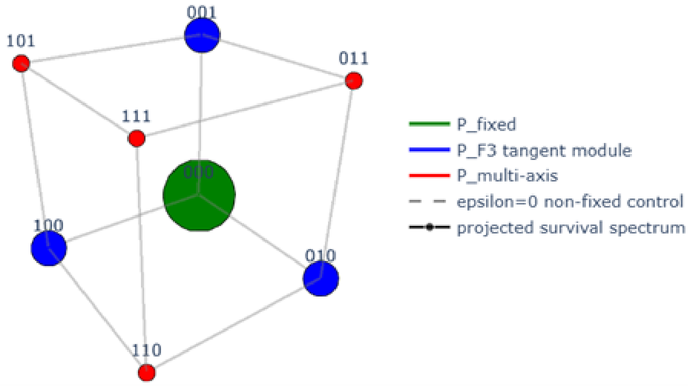

Figure 2. The eight orientation modes of the signed octahedral transport layer form the binary cube $\Gamma \simeq (\mathbb{Z}_2)^3$. The Walsh diagnostic organizes them into one invariant mode, three single-axis tangent modes and four higher multi-axis modes. Computed via [62].

The same script also computes the Walsh survival spectrum and the $\epsilon = 0$ transport-only control (not reproduced here). The invariant mode remains fixed, the non-invariant sectors are damped with a positive spectral gap, and disabling pole aliasing keeps the non-invariant content flat. The filtration is thus driven by finite-resolution pole aliasing, not by graph transport alone.

This generation carrier also has the right spectator structure for gauge labels. For a gauge representation V_R, the matter space takes the form $\mathcal{F}_3 \otimes V_R$. The gauge action acts only on V_R and leaves the three-dimensional generation carrier untouched. Equivalently, the gauge generators commute with the projectors onto the three generation slots. The same gauge representation can therefore sit over three identical slots without inserting three independent copies by hand. In compact form, the logic is

$$(\mathbb{Z}_2)^3 \xrightarrow{\text{Walsh}} (1,3,3,1) \Rightarrow \mathcal{F}_3 = \mathcal{W}_1 \Rightarrow \dim \mathcal{F}_3 = 3.$$

The module $\mathcal{F}_3$ is the generation carrier selected by the finite boundary update.

In this picture, "now" is the latest stable record after a CPTP update, and "time passing" is the irreversible sequence of such updates.

2.10. *Recovery of Standard Limits and Entropic Arrow of Time*

Einstein Limit. Standard limits follow directly by varying the unified matching-scale action obtained from the relative-entropy Hessian. In the infrared ($E \ll M_s$), the heat-kernel expansion matches onto the Einstein–Yang–Mills–Dirac Lagrangian with the locked $\lambda = M_P^2/(12M_s^2)$ coefficient in the reduced homogeneous curvature sector; as E approaches M_s, the continuum EFT loses operational resolution and is replaced by discrete boundary updates. For the gravitational sector, defining the effective stress-energy tensor $T_{\mu\nu}^{\text{eff}}$ via the standard metric variation of the matter action, the R^2 saturation term yields the corrected Einstein equations:

$$M_P^2 G_{\mu\nu} + \frac{M_P^2}{6M_s^2} H_{\mu\nu}^{(R^2)} = T_{\mu\nu}^{\text{eff}}, \qquad H_{\mu\nu}^{(R^2)} = 2RR_{\mu\nu} - \frac{1}{2} g_{\mu\nu} R^2 - 2\nabla_\mu \nabla_\nu R + 2g_{\mu\nu} \Box R.$$

In the low-curvature regime $|R| \ll M_s^2$ the higher-order correction is heavily suppressed (by powers of $|R|/M_s^2$). Stationarity of the variational functional constrains the background to the Einstein universality class [6,67], giving $M_P^2 G_{\mu\nu} \approx T_{\mu\nu}^{\text{eff}}$ with stiffness set by the extensive channel capacity N_{eff} [41].

Yang–Mills and Dirac Limits. The same structure matches the Yang–Mills response, while the spinorial transport sector supplies Dirac kinematics. The vector block is fixed by the quantized WZW current algebra (P6) together with the universal modular correlator $\langle J(\tau)J(0)\rangle \propto \sin^{-2}(\tau/2)$ evaluated on the $S^3 \times S^1$ history manifold; its quadratic response directly yields the gauge kinetic term and the Yang–Mills field equation $D_\mu F^{\mu\nu} = J^\nu$. Together with the scalar mass deformation, the spinorial transport block gives $(i\gamma^\mu D_\mu - m)\psi = 0$. These macroscopic equations emerge jointly from the boundary response. While entropic derivations of gravity are established [6,50], this finite-resolution architecture extends that emergence to the gauge and matter sectors. The required boundary completion, discrete transport and symmetry projections block-diagonalize the leading response, yielding the Einstein, Yang–Mills and Dirac equations as a unified output rather than independent postulates.

Hawking Scaling Limit. At macroscopic horizon scales, the open-boundary leakage picture is compatible with the standard Hawking scaling. Distinguishing the horizon surface gravity κ_H from the local tip impedance κ, one has $T_H = \kappa_H/(2\pi)$ and, for a four-dimensional Schwarzschild horizon, $A_H \propto \kappa_H^{-2}$. Hence the asymptotic thermal power scales as $P_\infty \sim A_H T_H^4 \propto \kappa_H^2$, up to greybody and species factors [44,77]. This shows that the finite-resolution CPTP update has the right local thermodynamic engine to reproduce the surface-gravity scaling of Hawking emission at macroscopic horizons.

Entropic Arrow of Time. Finite resolution (P5) supplies a structural basis for the arrow of time. Passing from one resolved diamond to the next coarse-grains over exiting data, inducing the CPTP map Φ on the resolved state ρ_{res}. In the Markovian update rule introduced above, the thermodynamic arrow of time arises from the contractivity of relative entropy under each CPTP step [37,78], ensuring that state distinguishability decreases monotonically across successive updates. When the reference is stationary, or when the same update acts on both state and reference, contractivity makes relative entropy decrease along the coarse-grained flow:

$$S_{\text{rel}}(\Phi(\rho) \| \Phi(\sigma)) \le S_{\text{rel}}(\rho \| \sigma) \quad \Longrightarrow \quad \left\langle \frac{dS_{\text{rel}}}{d\tau} \right\rangle \le 0.$$

As a result, the thermodynamic arrow of time (the irreversible loss of distinguishability) follows from the finite-resolution architecture and its Markovian update rule.

2.11. Universal Entropic Variational Principle (Conjecture)

Motivated by the construction above, we conjecture that the relative-entropy Hessian defines the emergent bulk metric under the continuum embedding. In this information-geometric picture, spacetime distance measures distinguishability: statistically similar boundary sources are geometrically close, while distinct ones are far apart. Because distinguishability can never be negative and only shrinks when information is lost, the emergent geometry inherits the positivity and monotonicity of the underlying Kubo–Mori metric governing linear response near equilibrium.

Identifying the relative-entropy Hessian with the Bogoliubov–Kubo–Mori monotone metric on the boundary sources Λ over $\mathfrak{A}_O$ gives the conjectural variational relation [78]:

$$\delta S_{\mathrm{rel}}(\rho_O \| \sigma_O[\Lambda]) = 0, \qquad g_{AB} = \frac{1}{M_s^2} \frac{\delta^2 S_{\mathrm{rel}}}{\delta \Lambda^A \delta \Lambda^B}\bigg|_{\mathfrak{A}_O}.$$

Here, A and B are DeWitt condensed source indices, subsuming resolved position, source type and internal tensor components into a single label. They parameterize the source space and define the target metric g_{AB}.

At the symmetric matched reference, this source-space metric is block-diagonal between inequivalent tensor, vector and scalar modules. This is a local tangent-space statement: away from the reference point, or at higher derivative order, suppressed off-block terms may appear as nonlinear EFT corrections.

In the macroscopic limit ($E \ll M_s$), the embedding maps these source directions to continuum field, tensor and gauge structures. Under this infrared mapping, the second variation reduces to the Kubo–Mori inner product on the continuous transport operator $D_{\mathcal{A}}$. Its heat-kernel expansion then matches onto the Einstein–Yang–Mills–Dirac action, including the locked Starobinsky coefficient $\lambda = M_P^2/(12M_s^2)$, the gauge coupling $\alpha^{-1}(M_s) = 4\pi k$ and the scalar mass deformations.

Although a computational implementation on the finite octahedral lattice is straightforward (representing $\mathfrak{A}_O$ as finite matrices, computing S_{rel} and its Hessian, solving $\delta S_{\mathrm{rel}} = 0$ by iteration), the formal continuum limit remains conjectural. The extracted metric g_{AB} is then coarse-grained below M_s to recover the matched continuum EFT. A rigorous proof requires three steps: (i) an embedding map from discrete transport operators to continuum fields preserving conformal structure, (ii) infrared convergence of the discrete Hessian to the continuous heat-kernel expansion and (iii) a controlled renormalization-group flow protecting the locked coefficient $\lambda = M_P^2/(12M_s^2)$.

Until that proof is formalized, the framework operates as a bipartite effective theory: a continuous effective action below M_s and a discrete algebraic update rule above M_s. Proving this universal conjecture forms the remaining open challenge; such a proof would establish a computationally finite, background-independent formulation of emergent semiclassical gravity.

3. Numerical Predictions Across Scales

This chapter summarizes the quantitative predictions derived in Appendices A–D from the core ingredients of Chapters 1 and 2. All entries are evaluated within the same finite-resolution container $(\mathcal{O}, \mathfrak{A}_O, \delta)$, where the relative-entropy Hessian separates the tensor, vector and scalar response sectors into a matching-scale problem.

The objective is to display the numerical consequences of this architecture in one place. The predictions span plateau cosmology, electroweak saturation, gauge stiffness, and charged-lepton spectral filtration. They are not split into isolated sector tables because their correlations are part of the claim: the same boundary capacity, coherence fraction and matching scale constrain sectors that are usually parametrized independently.

The numerical compression is central to the phenomenological content. Once the dimensionless boundary capacity $N \simeq 1.23 \times 10^{11}$ is fixed by the finite-resolution boundary geometry, Newton's constant is used once to calibrate the resolution scale,

$$G \longrightarrow M_s \simeq 3.02 \times 10^{13}\,\mathrm{GeV}.$$

After the minimal boundary sector is selected, the listed observables follow without continuous parameter fitting. This gives a high predictive compression across domains that, in conventional models, are normally described by many separately fitted continuous inputs.

The count is therefore organized by evidence groups rather than by table rows. The table contains 24 numerical rows, but 19 non-redundant phenomenological evidence groups. Dependent rows are explicitly labeled: the redundant plateau translation M_R relative to λ_{R^2}, the redundant inverse-coupling ratio $\alpha_{\rm em}^{-1}/\alpha_s^{-1}$, the bridge quantity $\mathcal{N}_*$, and the coupled diagnostics $[r, S_8, y_t, \lambda_H, \sin^2\theta_W]$.

These coupled diagnostics share parent mechanisms but confront distinct observational datasets. Specifically, the tensor ratio r is coupled to the scalar tilt n_s through the same plateau coherence duration $\mathcal{N}_*$. The growth estimate S_8 is coupled to the vacuum fraction $\Omega^{\rm IR}_{\Lambda,0}$ through the identical late-time leakage mechanism. The dimensionless electroweak quantities y_t and λ_H are rigid algebraic locks on the mass saturation outputs $(m^{(2)}_{\rm max}, v, m_H)$. Finally, the weak-mixing angle $\sin^2\theta_W$ evaluates the same normalized current embedding that fixes the UV gauge blocks. Because these rows introduce no new adjustable parameters, they are conservatively not counted as theoretically independent evidence groups. They remain, however, independent observational tests: the empirical failure of any single diagnostic would strictly falsify its parent mechanism.

Table 1 presents the resulting numerical audit.

Audit flag $[X, Y]$. The first entry gives the evidential role: P = primary target; C = coupled diagnostic; R = redundant translation; Q = bridge quantity. The second entry gives the non-redundant evidence group 1–19.

Table 1: Summary of Predictions vs. Observations

Quantity	Prediction	Observation	Deviation	Audit
Cosmology: Plateau Coherence, Capacity Limits and Entropic Response (Appendix A)				
Scalaron mass M_R	3.02×10^{13} GeV	3.00×10^{13} GeV [79]	0.7%	[R,1]
Plateau stiffness λ_{R^2}	5.42×10^8	5.44×10^8 [79]	0.4%	[P,1]
Coherence $\mathcal{N}_*$	$18\pi \simeq 56.55$	–	–	[Q,2]
Scalar tilt n_s	0.9646	0.9649 ± 0.0042 [79]	0.03%	[P,2]
Tensor ratio r	0.0038	< 0.036 [80]	Consistent	[C,2]
Scalar amplitude A_s	2.08×10^{-9}	$(2.10 \pm 0.03) \times 10^{-9}$ [79]	1.0%	[P,3]
BH threshold M_δ	2.46×10^{24} GeV	–	–	[P,4]
Vacuum $\Omega^{\rm IR}_{\Lambda,0}$	$4/6 \simeq 0.667$	0.689 ± 0.006 [81]	3.2%	[P,5]
Struct. growth S_8	0.816	0.76–0.84 [79,82]	Consistent	[C,5]
Accel. floor a_0	1.04×10^{-10} m s^{-2}	1.2×10^{-10} m s^{-2} [83,84]	Consistent	[P,6]
Electroweak Saturation Bounds and Consistency Checks (Appendix B)				
Higgs mass m_H	125.7 GeV	125.25 ± 0.17 GeV [81]	0.36%	[P,7]
VEV v	246.3 GeV	246.22 GeV [81]	0.03%	[P,8]
Top mass cap $m^{(2)}_{\rm max}$	174.1 GeV	172.69 ± 0.30 GeV [81]	0.8%	[P,9]
Top Yukawa y_t	1.00	0.99 ± 0.01 [81]	1.0%	[C,10]
Higgs quartic λ_H	0.130	0.126 ± 0.001 [81]	3.2%	[C,11]
Gauge Couplings as Entropic Stiffness (Appendix C)				
Strong $\alpha_s^{-1}(M_s)$	$12\pi \simeq 37.7$	$\simeq 38 \pm 2$ [81,85]	1%	[P,12]
EM $\alpha_{\rm em}^{-1}(M_s)$	$36\pi \simeq 113.10$	113.4 [85]	0.2%	[P,13]
Weak-mixing $\sin^2\theta_W$	0.375	0.38 [81,85]	1%	[C,14]
Internal lock $\alpha_{\rm em}^{-1}/\alpha_s^{-1}$	3	3.03 [85]	1%	[R,12–13]
Fine-structure $\alpha^{-1}(0)$	137.035999216	137.035999206(11) [86]	$< 10^{-10}$	[P,15]
Lepton Mass Spectrum via Spectral Filtration (Appendix D)				
Proton mass m_p	942 MeV	938 MeV [81]	0.4%	[P,16]
Electron mass m_e	0.511009 MeV	0.510999 MeV [81]	2×10^{-5}	[P,17]
Muon mass m_μ	104.25 MeV	105.66 MeV [81]	1.3%	[P,18]
Tau mass m_τ	1.788 GeV	1.777 GeV [81]	0.6%	[P,19]

4. Conclusions and Outlook

This work has developed a finite-resolution boundary formulation of semiclassical gravity. In a background-independent Wheeler-DeWitt quantum theory, the global state is constrained rather than time-evolved. There is no external clock, no pre-existing spacetime stage, and no clean factorization of local Hilbert spaces across subregions. The central operational problem is therefore not to quantize a bulk graviton on an assumed background, but to explain how an internal observer extracts time, locality and measurable physics from a non-factorizing universe.

We resolve this problem by defining a local subsystem through the finite records an observer can distinguish. The causal diamond provides the minimal covariant laboratory for this task. Diffeomorphism and Gauss-law constraints obstruct naive bulk factorization, so accessible subregion data must be tied to the closed boundary interface, the diamond waist S^2. Holographic bounds require this boundary to carry finite information capacity. Modular flow supplies the intrinsic clock. Boundary completion defines the measurable algebra. Finite resolution fixes the shared operator content. The physical state ρ_O and the semiclassical reference family $\sigma_O[\Lambda]$ can then be compared on the same algebra $\mathfrak{A}_O$.

The axioms P1–P7 formalize these operational requirements by defining subsystems, clocks, charges, transport, spinors and regulated observables, without a background spacetime or preferred lattice. Dynamics are then posed as local statistical inference, where relative entropy $S_{\mathrm{rel}}(\rho_O \| \sigma_O[\Lambda])$ measures the mismatch between boundary data and the reference, establishing the primitive objects not as bulk trajectories, but as finite relations on the boundary algebra.

The novelty of the framework lies in the order in which established structures are assembled. Boundary completion first fixes the algebra. Finite resolution fixes the bandwidth. Relative entropy supplies the variational principle. The Kubo–Mori Hessian supplies the response metric. Open modular updates supply the local arrow of time.

This order changes the structure of the problem. In standard effective-field descriptions, gravitational, gauge, scalar and cosmological parameters enter as independent continuous inputs. Here they arise as correlated outputs of one finite-resolution boundary sector. The same screen controls gravitational stiffness, gauge response, scalar saturation, plateau coherence and charged-lepton filtration. The framework is therefore not a collection of sector-by-sector fits. It is a constrained inference architecture whose numerical outputs are locked to the selected boundary topology and matching convention.

The crucial technical insight is the native orthogonal decoupling of the relative-entropy Hessian. At the matching scale, the leading quadratic response separates into tensor, vector and scalar blocks. This single object generates the response structure normally distributed across separate physical theories: the tensor block yields Einstein gravity and the R^2 plateau, the vector block yields Yang–Mills stiffness and the scalar blocks yield mass deformations and Dirac transport.

4.1. Finite Capacity and Origin of Hierarchy

The selected causal diamond, its closed boundary geometry, its modular routing structure and its spin-compatible transport fix the effective boundary channel multiplicity:

$$N = \sqrt{2}\exp\left(8\pi + \frac{1}{6\pi}\right) \simeq 1.23 \times 10^{11}.$$

This internal response capacity quantifies the exact, unavoidable cost of digitizing the continuum dictated by the axioms. The 8π coefficient is the global Gauss–Bonnet topological overhead required to close the finite S^2 interface (P1–P3). The $1/(6\pi)$ factor is the $L_2 \to L_1$ digitization cost at the sub-resolution tips, representing the unavoidable drop in coordination number at the poles averaged over one modular cycle (P4, P5). The $\sqrt{2}$ prefactor is the minimal twist defect lifting $SO(3)$ to $SU(2)$ to close the algebra under local frame transport, thereby supporting local spinors (P6–P7).

Only a coherent fraction of these channels participates in gravitational stiffness. The impedance factor κ selects the coherent tensor depth N_{eff}, which is then calibrated to Newton's constant to yield the single dimensional matching scale M_s:

$$\kappa = \frac{1}{6\pi}, \qquad N_{\mathrm{eff}} = \kappa N, \qquad M_s = \frac{M_P}{\sqrt{N_{\mathrm{eff}}}} \simeq 3.02 \times 10^{13}\,\mathrm{GeV}.$$

The Planck scale is therefore not the microscopic resolution scale. It is the collective macroscopic stiffness of N_{eff} coherent boundary response channels. Gravity is extensive in N_{eff}, while gauge and scalar responses remain intensive, per-pixel quantities. This extensive–intensive separation gives a structural origin for the hierarchy between the Planck scale and electroweak-scale saturation.

The picture is not a discretized spacetime with a graviton placed on top. It is a finite bundle of coherent response channels whose collective tensor response appears macroscopically as gravity.

4.2. *Unified Matching-Scale Action at M_s*

The relative-entropy response (Kubo–Mori Hessian) natively decouples into independent tensor, vector, and scalar blocks, generating distinct physical regimes: the tensor block yields gravity (Einstein–Hilbert stiffness and locked R^2 plateau), the vector block yields gauge interactions (Yang–Mills kinetic terms) and the scalar blocks supply matter (mass deformations, Dirac transport).

$$\mathcal{L}(M_s) = \frac{M_P^2}{2}R + \frac{M_P^2}{12M_s^2}R^2 - \frac{1}{4g(M_s)^2}F_{\mu\nu}F^{\mu\nu} + \bar{\psi}i\gamma^\mu D_\mu\psi - m\bar{\psi}\psi + \cdots .$$

This continuum Lagrangian is the $E < M_s$ response representative of the finite boundary theory.

4.3. *Open Modular Dynamics and Filtration of Matter*

Local time emerges from the discrete updating of the resolved causal diamond. Digitizing continuous modular flow onto a finite boundary graph (P4, P5, P7) unavoidably discards sub-resolution data. This irreducible loss forces local time evolution to be an inherently open Markov process. The resolved state updates by a completely positive trace-preserving (CPTP) map; in the Markovian limit, its generator takes GKSL form.

The arrow of time follows from relative-entropy contractivity under these updates. The “now” is the latest stable record, and time is the irreversible sequence of such records.

The same open update coarse-grains non-abelian symmetry data into commuting sectors ($G \to \mathfrak{g} \to T$). The octahedral transport layer carries the orientation group $\Gamma \simeq (\mathbb{Z}_2)^3$, whose Walsh decomposition splits the eight modes into $1+3+3+1$. The degree-one sector $\mathcal{W}_1$ uniquely isolates a three-dimensional carrier ($\dim \mathcal{F}_3 = 3$), providing an algebraic origin for the three generations of matter. This threefold structure is dynamically selected by the finite boundary update via an exact algebraic projection of the Walsh basis, rather than mere stage counting.

4.4. *Phenomenological Compression and Falsifiability*

As detailed in Chapter 3, the framework generates 24 numerical rows organized into 19 non-redundant phenomenological evidence groups. Coupled diagnostics such as r, S_8, y_t, λ_H and $\sin^2\theta_W$ share parent mechanisms but confront separate observables. They introduce no new parameters, so they test the internal consistency of their parent sectors without diluting predictive power. A failure of any coupled diagnostic would constrain, or falsify, the corresponding mechanism.

The resulting compression is strict. Rather than fitting separate variables for cosmology, electroweak saturation limits, gauge couplings and lepton masses, the framework organizes them as correlated outputs of the same boundary architecture. Once the dimensionless capacity N is fixed and Newton’s constant calibrates M_s, this entire phenomenological spectrum follows without continuous parameter fitting.

This rigidity is the framework’s main phenomenological strength, but also its primary vulnerability. Any robust empirical deviation across these sectors leaves no parametric room to adjust, directly falsifying the selected boundary topology.

4.5. *Universal Entropic Variational Principle (Conjecture)*

The conceptual core of the framework reduces to a single universal relation. Without it, the architecture remains a bipartite construction: discrete boundary inference in the UV, matched to an effective Laplacian and heat-kernel expansion in the IR.

The conjectured universal relation bridges these two regimes by defining the emergent source-space metric directly as the Hessian of relative entropy on the finite algebra:

$$\delta S_{\mathrm{rel}}(\rho_O \| \sigma_O[\Lambda]) = 0, \qquad g_{AB} = \frac{1}{M_s^2} \frac{\delta^2 S_{\mathrm{rel}}}{\delta\Lambda^A \delta\Lambda^B}\bigg|_{\mathfrak{A}_O}.$$

Here, A and B are DeWitt condensed indices subsuming resolved position, source type and internal tensor components into a single label parameterizing the macroscopic source space.

In the IR, this entropic metric reduces to the macroscopic Laplacian response. In the UV, it operates exactly on the discrete operator content before any continuum limit is taken. Consequently, macroscopic geometry emerges not as an independent background, but as the Fisher information metric of the boundary algebra; physical distance is realized as the operational distinguishability of resolved quantum states.

If proven, this conjecture unifies the discrete UV rules and continuum IR action into a single semiclassical quantum theory of gravity. The mathematical proof is non-trivial and requires a controlled embedding of the finite transport algebra into continuum fields, convergence of the discrete Hessian to the heat-kernel expansion, and a renormalization argument protecting the locked coefficients below M_s.

4.6. Computational Verifiability

To ensure rigorous numerical verifiability, the foundational mechanisms of this framework have been implemented in a dedicated Python toolbox [62]. The simulations explicitly instantiate octahedrally refined S^2 boundary meshes, dense Hessian matrices, variational response solvers, symmetry projections and CPTP update maps.

These computational tools independently check three core mechanisms: applying octahedral symmetry to a generic mixed response verifies, on finite representatives, the orthogonal tensor, vector and scalar decoupling predicted by the boundary architecture; finite-graph solvers confirm the corresponding quadratic inference problem is globally convex and spatially localized; and CPTP audits verify the $1 + 3 + 4$ Walsh survival hierarchy, utilizing transport-only controls to demonstrate that irreversible filtration is driven entirely by localized pole aliasing.

This makes the central mechanisms constructible and inspectable. Boundary construction, capacity bookkeeping, Hessian decoupling, quadratic inference, spectral projection, CPTP updating, Walsh filtration and control tests can all be implemented on finite representatives before taking any continuum limit. The toolbox does not prove the full continuum theory, but it turns the architecture into a reproducible and falsifiable computational program.

4.7. Outlook

Several domains remain open. The Universal Entropic Variational Principle requires a formal proof. The matter sector must still derive chirality, neutrino masses, flavor mixing, and Yukawa texture. The black-hole threshold M_δ bounds the semiclassical horizon but does not resolve evaporation. Late-time cosmological observables $(\Omega_\Lambda, S_8, a_0)$ remain exploratory.

Despite these open domains, the central result is clear. A finite-resolution, boundary-completed causal diamond is sufficient to generate semiclassical gravity, gauge response, scalar saturation, open time evolution, and a threefold matter carrier from a single axiomatic operational architecture. The essential ingredient is not a new particle, a background geometry, or a preferred lattice. It is the insistence that local physics is strictly inferred from a finite, background-independent algebra with fixed operator content.

The framework is constructive, translating background-independent inference into exact response observables. It is definitively rigid and fragile, leaving no room for continuous parameter tuning.

In this setting, the observed scales of nature emerge not as unrelated constants, but as the stable limits of what a finite-resolution semiclassical quantum theory of gravity can represent.

Funding: This research received no external funding.

Data Availability Statement: The original contributions presented in this study are included in the article. Further inquiries can be directed to the corresponding author.

Acknowledgments: During the preparation of this manuscript, the author used Gemini 3 and ChatGPT 5.2 for the purposes of language polishing and converting the manuscript from MS-Word to LaTeX. The author has reviewed and edited the output and takes full responsibility for the content of this publication.

Conflicts of Interest: Olivier Nusbaumer was employed by the company Kernkraftwerk Leibstadt AG (Leibstadt Nuclear Power Plant) in Switzerland. The author declares that the research was conducted in the absence of any commercial or financial relationships that could be construed as a potential conflict of interest.

Appendix A. Cosmology: Plateau Coherence, Capacity Limits and Entropic Response

This appendix applies the finite-resolution boundary architecture to the macroscopic cosmological horizon. In this setting, the observer's causal diamond is the local Hubble patch, and its S^2 waist acts as the apparent horizon on which entropic matching is performed.

The goal is to show how the same fixed boundary data that determine microscopic response sectors also constrain macroscopic gravitational observables. This approach is highly constrained: the primordial macroscopic response follows from the fixed boundary geometry, without introducing any tuned inflaton potential. The relevant inputs are the tip-defect parameter κ, the total channel capacity N and the coherent tensor depth $N_{\text{eff}} = \kappa N$ established in Chapter 1.

The primordial observables are organized into two operational chains:

$$\kappa \to \tau_{\text{coh}} \to \mathcal{N}_* \to (n_s, r), \qquad\qquad (N, \kappa, \mathcal{N}_*) \to A_s.$$

The first chain fixes the plateau duration and shape observables from the tip defect. The second fixes the scalar amplitude as a downstream test of finite capacity, precluding circular parameter fitting. Rather than using the observed A_s to tune the plateau duration $\mathcal{N}_*$, the framework derives both independently.

Alongside the primordial plateau sector, the same fundamental scale sets a semiclassical black-hole horizon threshold M_δ. The late-time IR quantities Ω_Λ, S_8 and a_0 are then treated as exploratory consequences of the open-modular update.

Appendix A.1. Plateau Stiffness and Finite-Resolution Saturation

As established in Chapter 2, the framework reproduces standard GR at intermediate curvatures ($|R| \ll M_s^2$). As the curvature approaches the physical resolution scale ($|R| \to M_s^2$), finite resolution bounds the response. The leading four-derivative completion is captured by the $R + R^2$ effective action, placing the dynamics in the Starobinsky plateau universality class [43].

The heat-kernel evaluation on the modular history manifold $S^3 \times S^1$ fixes the mass scale at which the scalar-curvature response reaches the finite-resolution saturation regime. Since the spectral trace is cut off at the physical resolution $\delta = M_s^{-1}$, the scalaron mass is locked directly to the matching scale [63,64]:

$$M_R = M_s \simeq 3.02 \times 10^{13}\,\text{GeV}.$$

(CMB-inferred plateau scale: $\sim 3.00 \times 10^{13}$ GeV [79]; Relative deviation: 0.7%).

Equivalently, through the standard plateau dictionary ($\lambda_{R^2} \equiv M_P^2/12M_R^2$), this translates to a dimensionless stiffness of:

$$\lambda_{R^2} = \frac{M_P^2}{12M_s^2} = \frac{N_{\text{eff}}}{12} \simeq 5.42 \times 10^8.$$

(CMB-inferred plateau stiffness: 5.44×10^8 [79]; Relative deviation: 0.4%).

Deriving this physical bound directly from the spectral geometry prevents circular parameter fitting. This matching isolates the homogeneous scalar-curvature (R^2) projection on $S^3 \times S^1$; it does not constrain anisotropic invariants, such as independent Ricci-squared or Weyl-squared terms.

Appendix A.2. Coherence Duration ($\mathcal{N}_*$)

The duration of the inflationary plateau is fixed by the stability time of the scalar-curvature mode. The relevant evolution is not a static combinatorial count, but a first-passage problem for phase coherence on the resolved boundary algebra. The finite-resolution tips generate an irreducible distinguishability increment encoded by the tip defect $\kappa = 1/(6\pi)$, distributed over the two tip bottlenecks and the $D = 3$ spatial transport axes.

Because CPTP maps cannot increase relative distinguishability, repeated resolved updates accumulate an irreversible loss of scalar-curvature phase information until one operational unit is reached [58,78]. The projected distinguishability increment per resolved modular update (and its resulting first-passage time) are therefore $\Delta^{\text{scalar}}_{\text{dist}} = \kappa/(2D)$ and $\tau_{\text{coh}} = 2D/\kappa$. Physical expansion time is obtained from modular time through $d\mathcal{N} = H\delta\, d\tau$. On the plateau, $M_R = M_s = \delta^{-1}$, $H \simeq M_R/2$ and $H\delta \simeq 1/2$. Therefore:

$$\mathcal{N}_* = H\delta\, \tau_{\text{coh}} = \frac{1}{2}\frac{2D}{\kappa} = \frac{D}{\kappa} = 18\pi \simeq 56.55.$$

The same result also has a discrete-geometric representation: $\mathcal{N}_*$ is the product of the 3 spatial transport axes, the 2π modular cycle and the inverse $1/3$ tip fraction, yielding 18π. The CPTP route gives the mechanism; the geometric route gives the architectural normalization. Their agreement is a nontrivial check. The eight signed orientation states enter the Walsh filtration of matter-sector structure, not the plateau coherence-time calculation.

Appendix A.3. Primordial Observables (n_s, r, A_s)

With $\mathcal{N}_* = 18\pi$ fixed, the correlated plateau shape observables are:

$$n_s = 1 - \frac{2}{\mathcal{N}_*} \simeq 0.9646, \qquad r = \frac{12}{\mathcal{N}_*^2} \simeq 0.0038.$$

The tensor ratio $r \simeq 0.0038$ is a sharp target for next-generation CMB B-mode searches [80,87].

The primordial amplitude serves as a finite-capacity diagnostic of the local de Sitter readout. The coarse-grained curvature signal averages over the N independent channels of the vacuum budget, so the variance scales as $1/N$ in the selected finite-capacity readout:

$$A_s = \frac{M_R^2 \mathcal{N}_*^2}{24\pi^2 M_P^2} = \frac{\mathcal{N}_*^2}{24\pi^2 \kappa N} = \frac{81\pi}{N} \simeq 2.1 \times 10^{-9}.$$

(CMB-inferred: $(2.10 \pm 0.03) \times 10^{-9}$ [79]; Relative deviation: 1.0%).

The absolute Newton calibration cancels exactly. Because the plateau duration $\mathcal{N}_*$ is already fixed, A_s cannot act as a free normalization parameter, precluding any phenomenological tuning. The shape observables and amplitude normalization follow from separate operational chains (cleanly partitioning the temporal κ and spatial N resolution limits). Thus, $A_s \propto N^{-1}$ emerges as the direct macroscopic imprint of finite boundary capacity: the primordial scalar signal is fundamentally a finite-resolution effect that vanishes in the continuous-spacetime, infinite-capacity limit $N \to \infty$.

Appendix A.4. Black-Hole Horizon Threshold (M_δ)

The finite-resolution scale also sets a breakdown criterion for classical black-hole horizons. A Schwarzschild geometry is semiclassical only while $r_s \gg \delta$. Setting $r_s = \delta = M_s^{-1}$ gives:

$$M_\delta = \frac{1}{2GM_s} = \frac{4\pi M_P^2}{M_s} = 4\pi N_{\text{eff}} M_s \approx 2.46 \times 10^{24}\,\text{GeV} \approx 4.4\,\text{g}.$$

This corollary illustrates how the framework converts the breakdown of semiclassical continuum horizon EFT into a concrete astrophysical mass scale, without adding new dynamical fields or tuning a remnant parameter. It is not a proof of a stable remnant; that requires a separate treatment of backreaction, evaporation and the discrete boundary update rule.

The plateau observables above follow from the fixed matching scale M_s, the short-time CPTP kernel and the horizon-entropy consistency ($S_0(A) = A/4G$) already established [34,44]. Extending this open-modular architecture to deep IR scales ($E \ll M_s$) requires interpolating the loss of distinguishability over cosmological baselines. The following late-time applications (Ω_Λ, S_8, a_0) are therefore classified as exploratory.

Appendix A.5. Late-time IR Horizon Leakage (Ω_Λ) (Exploratory)

In the deep IR, the horizon surface becomes informationally sparse. We model late-time vacuum energy not as a divergent bulk summation, but as the steady-state IR horizon leakage required to balance the finite-resolution open-modular update [2,88,89]. The same finite-resolution pole aliasing that sets the tip-defect scale in the UV supplies the local source of distinguishability loss, now projected onto the apparent horizon.

In this projection, the open-modular update supplies the leakage mechanism, while the late-time vacuum fraction is estimated from the active horizon-channel ratio. We have $z = 6$ signed transport directions and $\mathcal{C}_0 = 4$ active massless long-range species (2 photon polarizations + 2 graviton helicities). Because the late-time horizon temperature $T_H \sim H/(2\pi)$ is negligible compared to massive SM states, heavier species are thresholded out of the dissipative inventory, locking this active-channel count in the post-recombination epoch. As a result, the minimal leakage convention ($L_{\mathrm{IR}} = 1$) yields the minimal late-time vacuum-fraction target:

$$\Omega^{\mathrm{IR}}_{\Lambda,0} = L_{\mathrm{IR}} \frac{\mathcal{C}_0}{z} \xrightarrow{L_{\mathrm{IR}}=1} \frac{4}{6} \simeq 0.667.$$

(Observed: 0.689 ± 0.006 [81]; Relative deviation: 3.2%).

The value $L_{\mathrm{IR}} = 1$ is the minimal leakage convention of the selected IR implementation, not an independent derivation of the cosmological constant.

Appendix A.6. Horizon Coherence Loss and S_8 Suppression (Exploratory)

Evaluating the late-time kernel tests whether finite-resolution distinguishability loss inherently predicts the scale and direction of growth suppression. This suppression begins when the accumulated IR loss reaches one resolved unit. Beyond this threshold, the horizon-scale Kubo–Mori stiffness becomes lossy. Relative entropy is contractive under CPTP maps, so accessible large-scale distinguishability cannot increase once the unresolved boundary data have been discarded.

Because large-scale coherence dilutes isotropically over the physical spacetime volume, the survival factor f_{coh} is estimated with an inverse spacetime-dimension exponent, $\nu_{\mathrm{eff}} = 1/d = 1/4$. At the onset of vacuum domination, $H_*/H_0 = \sqrt{2\Omega_{\Lambda,0}}$. Substituting the framework's predicted $\Omega_{\Lambda,0} = 2/3$ gives $f_{\mathrm{coh}} = (H_0/H_*)^{\nu_{\mathrm{eff}}} \simeq 0.965$. Using the standard growth-index approximation with $\gamma \simeq 0.55$ [90] and the baseline $S_8^{\mathrm{Planck}} \simeq 0.832$, this yields:

$$S_8^{\mathrm{pred}} \approx S_8^{\mathrm{Planck}} f_{\mathrm{coh}}^{\gamma} \approx 0.816.$$

(Observed: 0.76–0.84 [79,82]; Consistent).

Appendix A.7. Entropic Horizon Acceleration Floor (a_0) (Exploratory)

A de Sitter-like horizon supplies the temperature scale $T_H \simeq \hbar H/(2\pi k_B)$ [91]. An observer with proper acceleration a sees the Unruh temperature $T_U = \hbar a/(2\pi c k_B)$ [5]. Equating the Unruh and de Sitter KMS temperatures establishes the kinematic scale $a \sim cH$. Averaging this horizon

Preprints.org (www.preprints.org) | NOT PEER-REVIEWED | Posted: 22 May 2026 doi:10.20944/preprints202601.1205.v5

noise over one full 2π modular orbit yields a modularly normalized phenomenological floor. For $H_0 \approx 70\,\mathrm{km\,s^{-1}\,Mpc^{-1}}$, this evaluates to:

$$a_0 = \frac{cH_0}{2\pi} \approx 1.04 \times 10^{-10}\,\mathrm{m\,s^{-2}}.$$

(Observed: $\approx 1.2 \times 10^{-10}\,\mathrm{m\,s^{-2}}$ [83,84]; Consistent).

An inertial acceleration signal below this scale is masked by the horizon-KMS background. Unlike static modifications of gravity, this floor evolves dynamically with redshift as $a_0(z) \propto H(z)$.

Appendix A.8. Structural Rigidity and Falsifiability

Inputs. Fundamental matching scale $M_s \approx 3.02 \times 10^{13}$ GeV; channel multiplicity $N \approx 1.23 \times 10^{11}$.

Outputs. Scalaron mass $M_R \approx 3.02 \times 10^{13}$ GeV; plateau stiffness $\lambda_{R^2} \simeq 5.42 \times 10^8$; coherence duration $\mathcal{N}_* = 18\pi$ (verified by the discrete-geometric dual-route check); scalar tilt $n_s \simeq 0.9646$; tensor ratio $r \simeq 0.0038$; scalar amplitude $A_s = 81\pi/N \simeq 2.1 \times 10^{-9}$; black-hole horizon threshold $M_\delta \approx 2.46 \times 10^{24}$ GeV; late-time vacuum fraction $\Omega^{\mathrm{IR}}_{\Lambda,0} \simeq 0.667$; structure growth parameter $S_8 \simeq 0.816$; entropic acceleration floor $a_0 \simeq 1.04 \times 10^{-10}\,\mathrm{m\,s^{-2}}$.

Falsifiability. Discovering any robust deviation from the (n_s, r, A_s) triad, specifically a broken $A_s = 81\pi/N$ capacity lock, a scalaron mass decoupled from the matching scale ($M_R \neq M_s$), or a missing $r \simeq 0.0038$ tensor signal, would falsify the minimal UV boundary model. Observing router-specific corrections to the $A/4G$ horizon entropy would invalidate the core architecture itself. At late times, measuring a vacuum fraction outside the 4/6 band, finding unsuppressed structure growth ($S_8 \approx S_8^{\mathrm{Planck}}$), or detecting a redshift-independent acceleration floor ($a_0 \not\propto H(z)$) would falsify the exploratory IR extension.

Appendix B. Electroweak Saturation Bounds

This appendix derives finite-resolution saturation relations for the electroweak scales m_H, v, and m_t, read out at the single-pixel activation scale E_{pix}. Numerical comparisons use standard SM scheme conventions [81].

The goal is to show how the finite capacity of a single boundary pixel rigidly dictates the electroweak mass scales. Rather than treating the Higgs potential and Yukawa couplings as free phenomenological inputs, the framework derives them purely from structural boundary limits.

These mass scales emerge as three complementary readouts of a single capacity bound: internal distinguishability, unresolved phase noise and gauge-invariant representability. They serve as consistency checks for the single-pixel cap, not as inputs to define it.

Appendix B.1. Per-Pixel Energy Budget (E_{pix})

The electroweak sector represents the saturation of the per-pixel boundary capacity, E_{pix}. This saturation is evaluated through the scalar block of the relative-entropy Hessian (Chapter 2) [38,39].

As explained in Chapter 1, the energy budget of a single boundary pixel is determined by its internal channel capacity N; because the $\mathbb{Z}_2$ spin-twist factor supplies a topological boundary grading rather than an independently addressable scalar state, it is excluded from the scalar occupancy count. Distributing the resolution scale M_s strictly across these available non-twist channels yields the single-pixel activation scale $E_{\mathrm{pix}} \approx 348.2$ GeV. Heavier localized excitations would require multi-pixel encoding.

Appendix B.2. Higgs Boson: Structural Entropic Cost

The Higgs field fixes the radial scale that converts internal electroweak charge directions into physical mass scales. Although three Goldstone directions do not remain as independent scalar modes at long distances, the regulated boundary algebra must represent the full $SU(2)$ doublet, with four real scalar components, to define the vacuum sector and normalize gauge charges under boundary completion.

Within the selected minimal sector, maintaining operational distinguishability of the four real doublet components against modular noise requires exactly one bit ($\ln 2$ in natural entropy units) per component ($\Delta S_H = 4\ln 2$) [92,93]. Intuitively, E_{pix} is the total scalar activation budget available to one resolved boundary pixel, while ΔS_H is the information load needed to represent the Higgs doublet on that pixel. The Higgs excitation cannot claim the full pixel budget as a single undivided mode; the boundary must first pay the binary distinguishability cost of the four scalar directions. The observable mass scale is the resulting activation energy per unit distinguishability cost: the larger the required internal bookkeeping, the smaller the mass gap supported by one pixel. This yields the structural mass relation:

$$m_H = \frac{E_{\text{pix}}}{\Delta S_H} = \frac{E_{\text{pix}}}{4\ln 2} \approx 125.7\ \text{GeV}$$

(Measured: 125.25 ± 0.17 GeV [81]; Relative deviation: 0.36%).

Appendix B.3. Vacuum Expectation Value: Noise Floor

The Vacuum Expectation Value (VEV) v represents the magnitude of the Higgs condensate (radial order parameter). At finite resolution, the internal scalar orientation is not stably locked against an external reference. The uniform modular phase average gives zero linear expectation (maximizing informational entropy [47]), while the stable radial order parameter is the RMS projection. With its maximum amplitude bounded by the pixel capacity E_{pix}, the VEV is:

$$v^2 = \langle (E_{\text{pix}} \cos\phi)^2 \rangle_\phi = \frac{1}{2}E_{\text{pix}}^2 \quad \to \quad v = \frac{E_{\text{pix}}}{\sqrt{2}} \approx 246.3\ \text{GeV}$$

(Inferred from G_F: 246.22 GeV [81]; Relative deviation: 0.03%).

Appendix B.4. Top Quark: Saturation Cap

Fermions cannot exist as isolated local observables (P1, P3) [11,13,18]; with edge completion, the minimal local scalar mass deformation is therefore a gauge-invariant dressed bilinear.

A single pixel must accommodate the total scalar insertion energy, so a q-leg operator assigns at most E_{pix}/q to each fermionic leg. This is governed by the single-pixel saturation cap $m_{\text{max}}^{(q)} = E_{\text{pix}}/q$. Mass deformations on the boundary-completed algebra must be closed, gauge-invariant scalar operators. A hypothetical single bare fermion ($q = 1$) is therefore inadmissible. The leading admissible mass deformation is the gauge-invariant bilinear $\bar{\psi}\psi$, fixing $q = 2$. Here $\bar{\psi}\psi$ denotes the scalar mass-density representative after boundary charge completion; in the chiral electroweak embedding, the corresponding closed operator is the Higgs-dressed Yukawa scalar [94], whose fermionic valence remains $q = 2$:

$$m_{\text{max}}^{(q)} = \frac{E_{\text{pix}}}{q} \xrightarrow{\bar{\psi}\psi,\, q=2} m_{\text{max}}^{(2)} = \frac{E_{\text{pix}}}{2} \approx 174.1\ \text{GeV}.$$

(Collider-extracted scale: 172.69 ± 0.30 GeV [81]; Relative deviation: 0.8%).

A small deviation of around one percent is expected for a quark, as strong quantum interactions inherently separate the experimental mass from the theoretical maximum [95].

Appendix B.5. Structural Locks and Vacuum Stability

The numerical comparisons use standard collider extraction and SM conversion conventions [81,95]. Physically, the vacuum does not select these masses; it simply bounds any excitation that attempts to exceed the per-pixel capacity of the regulated boundary (E_{pix}). This saturation condition fixes the dimensionless top and scalar couplings as rigid ratios:

$$y_t \equiv \frac{\sqrt{2}\, m_t}{v} \approx 1$$

Preprints.org (www.preprints.org) | NOT PEER-REVIEWED | Posted: 22 May 2026 doi:10.20944/preprints202601.1205.v5

(Inferred: 0.99 ± 0.01 [81]; Relative deviation: $\sim 1\%$).

$$\lambda \equiv \frac{m_H^2}{2v^2} = \frac{1}{16(\ln 2)^2} \approx 0.130$$

(Inferred: 0.126 ± 0.001 [81]; Relative deviation: 3.2%).

This difference is a natural consequence of scale evolution. As a high-energy boundary condition at M_s, the predicted coupling evolves down to the observed collider value, reproducing the established near-critical vacuum stability pattern [85,96].

Appendix B.6. Structural Rigidity and Falsifiability

Inputs. Fundamental matching scale M_s; internal channel capacity N (which dictate the single-pixel budget $E_{\text{pix}} = \sqrt{2}M_s/N$).

Outputs. Top quark saturation cap $m_{\text{max}}^{(2)} \approx 174.1$ GeV; Higgs boson mass $m_H \approx 125.7$ GeV; vacuum expectation value $v \approx 246.3$ GeV; top Yukawa coupling $y_t \approx 1$; Higgs quartic coupling $\lambda \approx 0.130$.

Falsifiability. This architecture would be falsified by any persistent violation of these relations after standard scheme conversion and RG evolution, the discovery of a heavier elementary single-pixel fermion within the same scalar sector, or a measured Higgs quartic incompatible with the predicted boundary condition.

Appendix C. Gauge Couplings as Entropic Stiffness

This appendix derives matching-scale gauge kinetic coefficients from the vector block of the relative-entropy Hessian on the boundary-completed algebra [57,59]. The derivation evaluates the vector response directly over the minimal boundary inventory established in Chapters 1 and 2.

The goal is to show that gauge couplings are not arbitrary free parameters, but emerge as quantized entropic stiffness coefficients.

The derivation follows a structural axiomatic chain: Non-factorization and Boundary Completion (P1, P3) dictate a boundary charge algebra; Modular Locality and Finite Resolution (P4, P5) define the modular susceptibility [11,16]; Gauge Topology (P6) fixes the admissible topological level k [21,24,69]; and the relative-entropy Hessian maps these discrete levels to the continuum gauge kinetic term.

The framework computes two distinct gauge observables from the same Hessian. The first is the local UV matching-scale relation $\alpha^{-1}(M_s) = 4\pi k$, which governs the intensive kinetic coefficient read by a single normalized current block. The second is the fully coarse-grained macroscopic static response $\alpha^{-1}(0)$.

The raw modular integral, the topological level, the quadratic inventory trace and the finite-capacity spectral sum are not competing prescriptions, but complementary readouts of this single boundary-completed vector Hessian.

Appendix C.1. Entropic Stiffness Quantization

We first establish the quantized boundary matching law that turns the vector-sector response into a definite gauge coupling at the matching scale. In Chapter 2, we extract the coupling by introducing a weak background gauge field in the KMS regime [4,18]. We then match the quadratic relative-entropy cost of this deformation to the standard Yang–Mills kinetic term. The Kubo–Mori Hessian [38,39,59] is evaluated in the Euclidean modular representation, mapping to the conventional Lorentzian macroscopic action by analytic continuation.

Microscopically, integrating the universal KMS current kernel $\langle \mathcal{J}(\tau)\mathcal{J}(0)\rangle \propto \sin^{-2}(\tau/2)$ over the resolved modular window $\tau \in [\epsilon, 2\pi - \epsilon]$ [24,69] yields an endpoint-dependent raw fluctuation. Dividing this raw readout by the universal modular-window factor cancels the endpoint dependence:

$$\chi_{\text{pix}}(\epsilon) = k\cot(\epsilon/2), \qquad I_{\text{mod}}(\epsilon) = 4\cot(\epsilon/2), \qquad \bar{\chi}_{\text{pix}} = \chi_{\text{pix}}/I_{\text{mod}} = k/4$$

Here, the first convergence of routes appears: the raw modular integral displays the universal KMS current kernel, while normalization removes its endpoint dependence to reveal the discrete level $k \in \mathbb{Z}$. This yields the quantized boundary matching law:

$$\alpha^{-1}(M_s) = 4\pi k, \quad k \in \mathbb{Z}$$

This result contains no hidden tuning parameters, holding at leading derivative order in the regime $\delta \ll \ell_O \ll R_{\rm curv}$ and $|p| \ll M_s$. The kinematic endpoint is a regularization artifact that exactly cancels; the boundary current algebra fixes the integer k, evaluated via the quadratic current metric over the boundary inventory; and 4π is the standard geometric flux factor for the closed S^2 interface.

Appendix C.2. Strong Sector Prediction ($k = 3$)

While topological consistency fixes the admissible gauge couplings to integer levels, the boundary matter inventory evaluates them in the selected sector. For the strong interaction with gauge group $SU(3)_c$, the problem is reduced to fixing one integer: $\alpha_s^{-1}(M_s) = 4\pi k_s$. The integer level is determined by one universal rule: the quadratic current metric $\mathrm{Tr}_{\mathcal{I}}$ evaluated over the shared boundary matter inventory $\mathcal{I}$.

The vector block extracts the parity-even gauge susceptibility. Its trace is therefore evaluated on completed Dirac color channels. Chiral imbalance belongs to parity-odd anomaly-inflow (not to the parity-even kinetic coefficient). For the selected strong sector, counting the six complete Dirac quark flavors yields $k_s = 6 \times T_{\mathrm{SU}(3)}(3) = 6 \times (1/2) = 3$ [97].

Remarkably, this matter trace evaluates exactly to the dual Coxeter number of the group ($h^\vee_{\mathrm{SU}(3)} = 3$), which characterizes the intrinsic non-Abelian self-interaction. This geometric equality $k_s = h^\vee_{\mathrm{SU}(3)}$ demonstrates that the bottom-up matter trace and the top-down geometric structure of the gauge group converge on the same integer. It thus recovers the intuition that strong-sector stiffness is structurally locked by the gauge group itself, even though the unifying operational rule remains the quadratic current trace. The matching-scale coupling follows immediately:

$$\alpha_s^{-1}(M_s) = 4\pi \cdot 3 = 12\pi \simeq 37.7$$

(SM RG Extrapolated Comparison at M_s: $\alpha_s^{-1} \simeq 38 \pm 2$ [81,85]; Relative Deviation: $\sim 1\%$)

Appendix C.3. Electromagnetic Prediction ($k = 9$) and Consistency Check

Just as the strong level k_s was fixed by the quadratic current metric, the Abelian level $k_{\rm em}$ is fixed by the same trace rule $\mathrm{Tr}_{\mathcal{I}}(Q^2)$. This equality enforces modular invariance on the $S^3 \times S^1$ history manifold. The effective boundary level $k_{\rm em}$ must balance the quadratic charge fluctuations of the matter fields to preserve the partition function. The electromagnetic stiffness thus acts as a topological counter-weight to the local charged inventory.

Normalizing Q to the positron charge, the minimal boundary inventory at M_s contains three fermion generations and one electroweak Higgs doublet. Expanding the trace over these components: quarks (3 colors $\times$ 3 generations $\times$ $[(2/3)^2 + (-1/3)^2]$) yield 5; charged leptons (3 generations $\times$ $(-1)^2$) yield 3; and the Higgs (the single complex charged component of the unbroken electroweak doublet at M_s) yields 1.

The total electromagnetic stiffness is the current-index sum $k_{\rm em} = 5 + 3 + 1 = 9$. This is a two-point quadratic current normalization, not a separate cubic anomaly trace or a perturbative beta-function coefficient. Spin-dependent loop weights enter the continuum RG comparison below M_s; they do not alter the representation trace defining the boundary current metric. The matching-scale coupling follows immediately:

$$\alpha_{\rm em}^{-1}(M_s) = 4\pi \times 9 = 36\pi \simeq 113.10$$

(SM RG Extrapolated Comparison at M_s: $\alpha_{\mathrm{SM}}^{-1} \approx 113.4$ [85]; Relative Deviation: $\sim 0.2\%$)

Within the electroweak current block, the same normalization yields the canonical weak-mixing projection. In the minimal embedding, the $SU(2)_L$ current and the canonically normalized hypercharge current share the same normalized level, $k_1 = k_2$. Using the matching relation $\alpha_i^{-1}(M_s) = 4\pi k_i$ and the standard hypercharge identity $\alpha_{\mathrm{em}}^{-1} = \alpha_2^{-1} + (5/3)\alpha_1^{-1}$, we obtain $\alpha_{\mathrm{em}}^{-1} = (8/3)\alpha_2^{-1}$. Inverting this ratio immediately fixes the weak-mixing angle:

$$\sin^2\theta_W(M_s) \equiv \alpha_{\mathrm{em}}/\alpha_2 = 3/8$$

(SM RG extrapolated comparison at M_s: ≈ 0.38 [81,85]; Relative deviation: $\sim 1\%$)

This recovers the canonical fermion ratio $\sum T_3^2/\sum Q^2$ [97,98] directly from boundary currents, without assuming simple-group unification.

Because both gauge sectors share the same 4π flux normalization, the ratio of inverse couplings depends only on the integers k. This boundary condition yields the internal consistency check known as the integer lock prediction:

$$\frac{\alpha_{\mathrm{em}}^{-1}(M_s)}{\alpha_s^{-1}(M_s)} = \frac{9}{3} = 3$$

(SM RG Extrapolated Comparison at M_s: ≈ 3.03; Relative Deviation: 1%)

Appendix C.4. Infrared Static Response: Fine-Structure Constant

The macroscopic on-shell static response $\alpha^{-1}(0)$ is the zero-frequency transverse Kubo–Mori susceptibility of the electromagnetic current [38,39,57], evaluated over the minimal compact history $S^3 \times S^1$ with pure-gauge zero modes factored out. The finite-capacity spectral trace inherently coarse-grains this response from the ultraviolet limit to the deep infrared. It provides a finite-capacity representation of the macroscopic polarization response that continuum EFT tracks through the step-by-step integration of resolved modes below M_s.

Just as hydrodynamics replaces microscopic collisions with effective constitutive laws, this spectral expansion packages unresolved quantum loops into exact geometric invariants [63,64,66,68].

Evaluated in the minimal boundary sector, the static trace introduces no free parameters. The electromagnetic projector is already locked by the ultraviolet matching law, $\alpha^{-1}(M_s) = 4\pi k$. With the local current normalization and flux convention fixed, the spectral trace collapses into a finite sum that computes the dimensionless macroscopic susceptibility of this exact same vector block. The calculation therefore reduces to the complete leading invariant set in the selected finite-capacity basis on the twisted, glued $S^3 \times S^1$ history manifold. Each term corresponds directly to an irreducible geometric feature of the causal diamond:

Bulk volume ($4\pi^3$). The axioms force the leading extensive term to equal the exact dimensionless volume of the resolved history manifold ($2\pi^2 \times 2\pi = 4\pi^3$) [63,99]. Physically, this counts the number of independent response channels across the full coherency screen: every modular update registers a local excitation that propagates once around the closed $S^3 \times S^1$ geometry (fixed by P2-P5). No other volume measure is compatible with the diamond construction.

Twist sector ($\pi^2 + \pi$). The spinorial lift required by discrete isotropic transport (P7) imposes a $\mathbb{Z}_2$ grading on closed loops around the screen. This grading forces a twisted sector in the heat-kernel trace; the half-measures $\pi^2 + \pi$ appear directly once the double-cover identification is imposed [63]. Physically, this registers the extra phase cost that fermions acquire when their worldlines wind once around the screen.

Gluing penalty ($-1/32\pi^4$). Algebraic completion of the subregion algebra (P3) glues past and future light cones across the waist S^2. The Gauss–Bonnet budget on that closed 2-sphere supplies a fixed capacity $\mathrm{Cap} = 8\pi$ (Chapter 1) [29]. The monotone-penalty rule isolates the unique leading interface suppression $-1/(\mathrm{Vol}\cdot\mathrm{Cap})$, appearing at order π^{-4}. This matches standard interface heat-kernel methods [100,101], encoding the irreducible cost of reconciling overlapping histories into a single operational record. Intuitively, because this reconciliation is not paid locally but globally across the closed S^2 ledger, the suppression is diluted by both history volume and boundary capacity, yielding the denominator $4\pi^3 \times 8\pi = 32\pi^4$.

Defect correction ($1/64\pi^6$). The transport-axis redundancy corollary fixes six transport directions on the screen ($z = 6$). At the diamond tips, the transverse cross-section drops below resolution, incurring a modular-closure overhead of $(2\pi)^{-6} = 1/(64\pi^6)$ that originates from the same finite-resolution tip-router structure defining κ, but it is not κ itself. Physically, this registers the coordination penalty paid every time an excitation traverses a sub-resolution bottleneck on the coherency screen.

These four contributions add linearly because each is a dimensionless geometric contribution to the same static heat-kernel response, with the normalization fixed by the matching-scale vector block. In the selected finite-capacity invariant basis, standalone inverse powers such as π^{-1} and π^{-2} are inadmissible because they violate the non-factorization rule (P1). Admissible corrections must form completed boundary invariants: the leading interface correction couples the history four-volume to the closed boundary capacity, while the leading transport correction couples to the finite six-axis defect. Terms built solely from single-scale factors are excluded by the Monotone Spectral Suppression rule (P5).

The powers 32 and 64 arise directly from the discrete bookkeeping of the coherency screen ($\mathrm{Vol}(S^3 \times S^1) \cdot \mathrm{Cap}(S^2)$ for the gluing interface and the six-axis closure $(2\pi)^{-6}$ for the tip defect), making the small corrections the irreducible boundary signatures that survive coarse-graining.

This yields the exact macroscopic static response for the fine-structure constant:

$$\boxed{\alpha^{-1}(0) = 4\pi^3 + \pi^2 + \pi - \frac{1}{32\pi^4} + \frac{1}{64\pi^6} \approx 137.035\,999\,216}$$

(Measured: $137.035\,999\,206(11)$ [86]; Relative Deviation $\approx 7 \times 10^{-11}$, $< 1\sigma$)

The two most precise measurements of α ([86] and [102]) differ by more than 5σ. Our approach discriminates between them:

$$\text{LKB 2020 (Rb) [86]: } 137.035\,999\,206(11) \rightarrow \text{ Agreement } (< 1\sigma)$$
$$\text{Berkeley 2018 (Cs) [102]: } 137.035\,999\,046(27) \rightarrow \text{ Disfavored } (> 5\sigma)$$

Our approach supports the LKB 2020 result [86], also acting as a falsifier.

This precision emerges from structural rigidity rather than parameter tuning. The coupling is evaluated globally as a coarse-grained vacuum stiffness rather than a perturbative loop series. Any alteration to the minimal inventory or history topology would shift the discrete spectral coefficients at order unity. The macroscopic response is therefore a strict, falsifiable postdiction of the underlying boundary geometry.

Appendix C.5. Structural Rigidity and Falsifiability

Inputs. Fundamental matching scale M_s; minimal SM matter inventory (3 generations, 1 Higgs doublet).

Outputs. Strong coupling $\alpha_s^{-1}(M_s) = 12\pi$ ($k_s = 3$); electromagnetic coupling $\alpha_{\mathrm{em}}^{-1}(M_s) = 36\pi$ ($k_{\mathrm{em}} = 9$); integer lock ratio $\alpha_{\mathrm{em}}^{-1}/\alpha_s^{-1} = 3$; weak mixing angle $\sin^2\theta_W(M_s) = 3/8$; fine-structure constant $\alpha^{-1}(0) \approx 137.035\,999\,216$.

Falsifiability. Any undiscovered charged particle content below M_s (which would alter the boundary current trace or break the RG-extrapolated integer lock); future metrology robustly favoring the Berkeley (Cs) recoil measurement [102] over LKB (Rb) [86].

Appendix D. Lepton Mass Spectrum via Spectral Filtration

This appendix derives the mass spectrum of the charged leptons through constrained spectral-accessibility on the Walsh carrier. Chirality, Yukawa textures, mixing and neutrino masses remain outside the scope. We adopt the algebraic structures established in Chapter 2, namely the Walsh generation carrier $\mathcal{F}_3 = \mathcal{W}_1$ and the separation of the composite multi-axis sectors $\mathcal{W}_{\geq 2} = \mathcal{W}_2 \oplus \mathcal{W}_3$ from the degree-one carrier. The mass denominators are given by the spectral accessibility Ω, restricted by finite boundary capacity [16,19] to an operationally accessible phase volume.

The goal is to show that the charged-lepton masses are not arbitrary free parameters, but that their hierarchy emerges as a sequence of geometric filtrations (full, tangent, commuting) of the finite, Lie-theoretical spectral accessibility. Using the Walsh transform [17,22] to isolate simultaneous family slots, we show in Chapter 2 that these filtrations are not empirical stage-counting, but three distinct geometric restrictions applied to the exact same spatial carrier.

The finite-mesh diagnostic [62] separates the causal diamond's spatial base from its internal symmetry fiber. Within the boundary algebra's principal-bundle structure [11,13,30], the spatial base supplies the transport redundancies ($\Gamma \simeq (\mathbb{Z}_2)^3$ and $\mathcal{F}_3$), while the internal fiber ($\mathcal{M}_{\text{int}}$) governs the mass gaps. This finite-resolution architecture recasts generations as spatial transport redundancies, and mass as the relative-entropy susceptibility of the internal fiber.

Appendix D.1. Proton Mass m_p (Dressed Hadronic Anchor)

The dressed non-abelian mass anchor for ordinary stable matter is the proton (m_p). The boundary dynamics should naturally reproduce this hadronic scale through confinement physics [103].

The confinement scale Λ_{QCD} is generated by running the strong coupling from M_s down to the pole, driven by the coupling $\alpha_s^{-1}(M_s) = 12\pi$ established in Appendix C [68]. Using a 1-loop beta function ($\langle b_0 \rangle \approx 7.25$ for effective running):

$$\Lambda_{\text{QCD}} \approx M_s \cdot \exp\left[-\frac{2\pi(12\pi)}{\langle b_0 \rangle}\right] \approx 200 \text{ MeV}$$

Following standard phenomenological models [104], we geometrically model the proton as the ground state of a spherical confinement cavity of radius $R \sim \Lambda_{\text{QCD}}^{-1}$. The lowest semiclassical orbital mode for a confined massless fermion gives the geometric eigenvalue $x_{1,-1} \approx 3\pi/2$. Thus, the cavity fundamental sets the mass scale:

$$m_p \approx \frac{3\pi}{2}\Lambda_{\text{QCD}} \approx 942 \text{ MeV}$$

(PDG value: 938 MeV [81]; Relative deviation $\sim 0.4\%$).

While the framework successfully derives m_p from the strong coupling, we use its empirical value to anchor the subsequent lepton estimates. This prevents QCD cavity-model uncertainties from propagating, keeping m_p strictly as the dressed non-abelian reference scale for the internal fiber.

Appendix D.2. Charged-Lepton Mass Spectrum

The matter space is taken as $\mathcal{H}^{(R)}_{\text{matter}} = \mathcal{F}_3 \otimes V_R$. Intuitively, $\mathcal{F}_3$ labels the three Walsh family slots, while V_R carries the gauge and spin representation. Since the gauge action is $I_{\mathcal{F}_3} \otimes \pi_R(X)$, it acts only on V_R and commutes with the family projectors P_i. The same gauge representation can therefore sit over the three family labels without inserting three independent copies by hand. Following the open modular dynamics and spectral filtration established in Chapter 2, $\mathcal{W}_2$ is not retained as a parallel carrier because it is a composite two-axis sector dynamically separated from $\mathcal{W}_1$ by the Hamming-degree spectral gap.

This dynamic separation is corroborated by the supplementary simulation toolbox (*open_modular_lie_filtration.py*) [62], which tracks CPTP polar aliasing on a finite S^2 mesh and confirms the $1+3+4$ Walsh survival hierarchy: the four multi-axis modes decay strictly faster than the three single-axis modes of $\mathcal{W}_1$, computationally validating the isolated generation carrier.

The boundary-to-spinor correspondence gives the internal chain $SO(3) \to SU(2) \to S^3$. This chain fixes the spinorial fiber used in the susceptibility estimate; it does not count the family slots. For the selected gauge/spinorial sector, the internal fiber is represented by $\mathcal{M}_{\text{int}} \cong S^3 \times S^5$.

As established in Chapter 2, the scalar block of the Kubo-Mori Hessian measures the susceptibility of this internal fiber [38,39,57]. Equivalently, the same rule is the Weyl-counting form of scalar susceptibility [63,64,99]: a larger accessible internal phase volume gives more low-energy response channels and therefore a softer mass gap, yielding $m_\ell \sim \text{reference scale}/\Omega_{\text{int}}^{(\ell)}$.

Full group access and tangent-generator access retain non-abelian dressing, so the electron and muon estimates use m_p. The commuting Cartan limit is pixel-bound, so the tau estimate uses the single-pixel energy budget $E_{\text{pix}} \simeq 348$ GeV established in Chapter 1. This baseline assignment applies strictly to charged leptons; quarks are not asymptotic isolated states and require a separate hadronic spectroscopy treatment.

Interestingly, the same susceptibility rule can be read in three complementary ways. In the full-accessibility limit, it becomes a Weyl phase-volume count on the internal fiber. In the tangent limit, it becomes a local generator count. In the commuting limit, it becomes a Cartan phase-volume count, with redundant orientation labels quotiented by $|\Gamma|$. These are not three generation stages; they are three internal readouts assigned over the already-selected Walsh carrier $\mathcal{F}_3$.

A useful intuition is ordinary navigation. Full internal-fiber accessibility is like a complete city map revealing both local streets and global topology. Tangent-generator accessibility is like standing at a single intersection: one sees the allowed directions, but the global layout is lost. Commuting Cartan accessibility restricts movement to independent circular tracks: one can travel continuously around each separate loop, but the intersections that allow complex, non-commuting turns are gone.

Electron (full internal-fiber accessibility). In this full-accessibility limit, the leading Weyl term fixes the dependence on the total internal phase volume; the Walsh factor then enters only through $\dim \mathcal{F}_3 = 3$. With the unit internal-fiber normalization used throughout the matching calculation, $\text{Vol}(S^3 \times S^5) = \text{Vol}(S^3)\,\text{Vol}(S^5) = 2\pi^2 \cdot \pi^3 = 2\pi^5$:

$$\Omega_e = \dim \mathcal{F}_3 \ \text{Vol}(S^3 \times S^5) = 3 \cdot 2\pi^5 = 6\pi^5, \qquad m_e = \frac{m_p}{6\pi^5} \approx 0.511009 \text{ MeV}.$$

(PDG: 0.510999 MeV [81]; Relative deviation $\approx 2 \times 10^{-5}$).

Muon (tangent-generator accessibility). This is the local, Lie-algebraic readout of the same internal fiber: it sees tangent directions, not the global phase volume. For the selected $SU(2)$ spinorial sector, $\dim \mathfrak{su}(2) = 3$ [97], so:

$$\Omega_\mu = \dim \mathcal{F}_3 \ \dim \mathfrak{su}(2) = 3 \cdot 3 = 9, \qquad m_\mu = \frac{m_p}{9} \approx 104.25 \text{ MeV}.$$

(PDG: 105.66 MeV [81]; Relative deviation $\approx 1.3\%$).

The relative deviation is consistent with the tangent-proxy character of this assignment.

Tau (commuting internal-fiber accessibility). The Cartan limit is the abelian readout of the internal fiber: phase information remains, but non-commuting dressing no longer participates in the accessible susceptibility volume. In this commuting pixel-bound limit, the relevant accessibility is the Cartan phase volume of the selected internal readout, represented by the unit four-torus T^4 [30], quotiented by the redundant orientation labels $|\Gamma| = 8$:

$$\Omega_\tau = \frac{\text{Vol}(T^4)}{|\Gamma|} = \frac{(2\pi)^4}{8} = 2\pi^4, \qquad m_\tau = \frac{E_{\text{pix}}}{2\pi^4} \approx 1.788 \text{ GeV}.$$

(PDG value: 1.777 GeV [81]; Relative deviation $\sim 0.6\%$).

This Cartan limit concerns the internal fiber and must not be confused with the spatial Walsh invariant sector $\mathcal{W}_0$.

Appendix D.3. Structural Rigidity and Falsifiability

Inputs. Fundamental matching scale M_s; pixel energy E_{pix}.

Outputs. Proton mass m_p (derived, then acting as the hadronic anchor); electron mass m_e; muon mass m_μ; tau mass m_τ.

Falsifiability. The framework is falsified by discovering a fourth chiral SM generation, which cannot fit the strictly three-dimensional Walsh carrier. The carrier mechanism is falsified if the finite-boundary CPTP update fails to isolate $\mathcal{W}_1$, the $\epsilon = 0$ control also contracts non-invariant content, or the Hamming-degree gap disappears. The mass estimates are falsified if the charged-lepton masses prove incompatible with the internal accessibility values $(6\pi^5, 9, 2\pi^4)$ once m_p and $E_{\rm pix}$ are fixed. Pure spatial S^2 pixel counts do not falsify these mass ratios, because $\Omega_{\rm int}$ is defined on the internal fiber, not the spatial screen.

References

1. DeWitt, B.S. Quantum Theory of Gravity. I. The Canonical Theory. *Phys. Rev.* **1967**, *160*, 1113–1148. https://doi.org/10.1103/PhysRev.160.1113.
2. Bousso, R. The Holographic Principle. *Rev. Mod. Phys.* **2002**, *74*, 825–874, [hep-th/0203101]. https://doi.org/10.1103/RevModPhys.74.825.
3. Page, D.N.; Wootters, W.K. Evolution without evolution: Dynamics described by stationary observables. *Phys. Rev. D* **1983**, *27*, 2885–2892. https://doi.org/10.1103/PhysRevD.27.2885.
4. Bisognano, J.J.; Wichmann, E.H. On the duality condition for a Hermitian scalar field. *J. Math. Phys.* **1975**, *16*, 985–1007. https://doi.org/10.1063/1.522605.
5. Unruh, W.G. Notes on black hole evaporation. *Phys. Rev. D* **1976**, *14*, 870. https://doi.org/10.1103/PhysRevD.14.870.
6. Jacobson, T. Thermodynamics of Spacetime: The Einstein Equation of State. *Phys. Rev. Lett.* **1995**, *75*, 1260–1263, [gr-qc/9504004]. https://doi.org/10.1103/PhysRevLett.75.1260.
7. Van Raamsdonk, M. Building up spacetime with quantum entanglement. *Gen. Relativ. Gravit.* **2010**, *42*, 2323–2329. https://doi.org/10.1007/s10714-010-1034-0.
8. Padmanabhan, T. Dark Energy and Gravity. *Gen. Relativ. Gravit.* **2008**, *40*, 529–564. [Class. Quant. Grav. 25, 205021 (2008)], https://doi.org/10.1007/s10714-007-0555-y.
9. Verlinde, E.P. Emergent Gravity and the Dark Universe. *SciPost Phys.* **2017**, *2*, 016, [arXiv:hep-th/1611.02269]. https://doi.org/10.21468/SciPostPhys.2.3.016.
10. Lashkari, N.; McDermott, M.B.; Van Raamsdonk, M. Gravitational dynamics from entanglement "thermodynamics". *Journal of High Energy Physics* **2014**, *2014*, 195, [arXiv:hep-th/1308.3716]. https://doi.org/10.1007/JHEP04(2014)195.
11. Donnelly, W.; Freidel, L. Local subsystems in gauge theory and gravity. *JHEP* **2016**, *09*, 102, [arXiv:hep-th/1601.04744]. https://doi.org/10.1007/JHEP09(2016)102.
12. Giddings, S.B. Hilbert space structure in quantum gravity: an algebraic perspective. *JHEP* **2015**, *12*, 099, [arXiv:hep-th/1503.08207]. https://doi.org/10.1007/JHEP12(2015)099.
13. Freidel, L.; Geiller, M.; Pranzetti, D. Edge modes of gravity. Part I. Corner potentials and charges. *JHEP* **2020**, *11*, 026, [arXiv:hep-th/2006.12527]. https://doi.org/10.1007/JHEP11(2020)026.
14. David, J.R.; Mukherjee, J. Entanglement entropy of gravitational edge modes. *JHEP* **2022**, *05*, 150, [arXiv:hep-th/2201.06043]. https://doi.org/10.1007/JHEP05(2022)150.
15. Bianchi, E.; Myers, R.C. On the architecture of spacetime geometry. *Classical and Quantum Gravity* **2014**, *31*, 214002, [arXiv:hep-th/1212.5183]. https://doi.org/10.1088/0264-9381/31/21/214002.
16. Susskind, L. The World as a Hologram. *J. Math. Phys.* **1995**, *36*, 6377–6396, [hep-th/9409089]. https://doi.org/10.1063/1.531249.
17. Nielsen, M.A.; Chuang, I.L. *Quantum Computation and Quantum Information: 10th Anniversary Edition*; Cambridge University Press: Cambridge, UK, 2010. https://doi.org/10.1017/CBO9780511976667.
18. Haag, R. *Local Quantum Physics: Fields, Particles, Algebras*; Springer-Verlag: Berlin, Heidelberg, 1992.
19. Bekenstein, J.D. Universal upper bound on the entropy-to-energy ratio for bounded systems. *Phys. Rev. D* **1981**, *23*, 287–298. https://doi.org/10.1103/PhysRevD.23.287.
20. Solodukhin, S.N. Entanglement Entropy of Black Holes. *Living Rev. Relativ.* **2011**, *14*. https://doi.org/10.12942/lrr-2011-8.
21. Witten, E. Quantum Field Theory and the Jones Polynomial. *Communications in Mathematical Physics* **1989**, *121*, 351–399. https://doi.org/10.1007/BF01217730.

22. D'Ariano, G.M.; Perinotti, P. Derivation of the Dirac equation from principles of information processing. *Phys. Rev. A* **2014**, *90*, 062106.
23. Deser, S.; Jackiw, R.; Templeton, S. Topologically Massive Gauge Theories. *Annals of Physics* **1982**, *140*, 372–411. https://doi.org/10.1016/0003-4916(82)90164-6.
24. Elitzur, S.; Moore, G.W.; Schwimmer, A.; Seiberg, N. Remarks on the Canonical Quantization of the Chern-Simons-Witten Theory. *Nucl. Phys. B* **1989**, *326*, 108–134. https://doi.org/10.1016/0550-3213(89)90436-7.
25. Susskind, L.; Thorlacius, L.; Uglum, J. The stretched horizon and black hole complementarity. *Physical Review D* **1993**, *48*, 3743–3761. https://doi.org/10.1103/PhysRevD.48.3743.
26. Bialynicki-Birula, I. On the Wave Function of the Photon. *Acta Phys. Pol. A* **1994**, *86*, 97–116. https://doi.org/10.12693/APhysPolA.86.97.
27. 't Hooft, G. Deterministic Quantum Mechanics: The Mathematical Equations. *Nucl. Phys. B* **2019**, *946*, 114703. https://doi.org/10.1016/j.nuclphysb.2019.114703.
28. Regge, T. General relativity without coordinates. *Il Nuovo Cimento (1955-1965)* **1961**, *19*, 558–571. https://doi.org/10.1007/BF02733201.
29. do Carmo, M.P. *Differential Geometry of Curves and Surfaces*; Prentice-Hall, 1976.
30. Nakahara, M. *Geometry, Topology and Physics*, 2 ed.; Graduate Student Series in Physics, Institute of Physics Publishing: Bristol and Philadelphia, 2003. Second edition, originally published 1990.
31. Kitaev, A.; Preskill, J. Topological Entanglement Entropy. *Phys. Rev. Lett.* **2006**, *96*, 110404, [hep-th/0510092]. https://doi.org/10.1103/PhysRevLett.96.110404.
32. Levin, M.; Wen, X.G. Detecting Topological Order in a Ground State Wave Function. *Phys. Rev. Lett.* **2006**, *96*, 110405, [cond-mat/0510613]. https://doi.org/10.1103/PhysRevLett.96.110405.
33. Kitaev, A. Anyons in an exactly solved model and beyond. *Annals of Physics* **2006**, *321*, 2–111. https://doi.org/10.1016/j.aop.2005.10.005.
34. Bekenstein, J.D. Black holes and entropy. *Phys. Rev. D* **1973**, *7*, 2333–2346. https://doi.org/10.1103/PhysRevD.7.2333.
35. 't Hooft, G. Dimensional Reduction in Quantum Gravity. *Conf. Proc. C* **1993**, *930308*, 284–296, [gr-qc/9310026].
36. Gorini, V.; Kossakowski, A.; Sudarshan, E.C.G. Completely positive dynamical semigroups of N-level systems. *Journal of Mathematical Physics* **1976**, *17*, 821–825.
37. Lindblad, G. On the generators of quantum dynamical semigroups. *Communications in Mathematical Physics* **1976**, *48*, 119–130.
38. Kubo, R. Statistical-Mechanical Theory of Irreversible Processes. I. General Theory and Simple Applications to Magnetic and Conduction Problems. *J. Phys. Soc. Jpn.* **1957**, *12*, 570–586. https://doi.org/10.1143/JPSJ.12.570.
39. Mori, H. Transport, Collective Motion, and Brownian Motion. *Progress of Theoretical Physics* **1965**, *33*, 423–455. https://doi.org/10.1143/PTP.33.423.
40. Sakharov, A.D. Vacuum quantum fluctuations in curved space and the theory of gravitation. *Dokl. Akad. Nauk SSSR* **1967**, *177*, 70–71. [Gen. Rel. Grav. 32, 365 (2000)].
41. Dvali, G. Black Holes and Large N Species Solution to the Hierarchy Problem. *Fortsch. Phys.* **2010**, *58*, 528–536, [0706.2050]. https://doi.org/10.1002/prop.201000009.
42. Minkowski, P. $\mu \to e\gamma$ at a rate of one out of 10^9 muon decays. *Phys. Lett. B* **1977**, *67*, 421–428. https://doi.org/10.1016/0370-2693(77)90435-X.
43. Starobinsky, A.A. A New Type of Isotropic Cosmological Models Without Singularity. *Phys. Lett. B* **1980**, *91*, 99–102. https://doi.org/10.1016/0370-2693(80)90670-X.
44. Hawking, S.W. Particle creation by black holes. *Commun. Math. Phys.* **1975**, *43*, 199–220. https://doi.org/10.1007/BF02345020.
45. Oriti, D.; Pranzetti, D.; Sindoni, L. Horizon entropy from quantum gravity condensates. *Physical Review Letters* **2016**, *116*, 211301, [arXiv:gr-qc/1510.06991]. https://doi.org/10.1103/PhysRevLett.116.211301.
46. Connes, A.; Rovelli, C. Von Neumann algebra automorphisms and time-thermodynamics relation in general covariant quantum theories. *Class. Quant. Grav.* **1994**, *11*, 2899–2917. https://doi.org/10.1088/0264-9381/11/12/007.
47. Jaynes, E.T. Information Theory and Statistical Mechanics. *Physical Review* **1957**, *106*, 620–630. https://doi.org/10.1103/PhysRev.106.620.
48. Frieden, B.R. *Physics from Fisher Information: A Unification*; Cambridge University Press, 1998.

49. Araki, H. Relative Hamiltonian for states of von Neumann algebras. *Publications of the Research Institute for Mathematical Sciences* **1976**, *11*, 809–833.
50. Verlinde, E. On the Origin of Gravity and the Laws of Newton. *JHEP* **2011**, *04*, 029, [arXiv:hep-th/1001.0785]. https://doi.org/10.1007/JHEP04(2011)029.
51. Bianconi, G. Quantum entropy couples matter with geometry. *J. Phys. A: Math. Theor.* **2024**, *57*, 365002. https://doi.org/10.1088/1751-8121/ad6f7e.
52. Bianconi, G. Gravity from entropy. *Phys. Rev. D* **2025**, *111*, 066001, [arXiv:gr-qc/2408.14391]. https://doi.org/10.1103/PhysRevD.111.066001.
53. Erdem, R. A review of some recent developments in the thermodynamics of gravity. *Turk. J. Phys.* **2022**, *46*, 51–69. https://doi.org/10.55730/1300-0101.2691.
54. Saridakis, E.N. Bouncing cosmology in entropic gravity. *Eur. Phys. J. C* **2024**, *84*, 1076. https://doi.org/10.1140/epjc/s10052-024-13455-5.
55. Sheykhi, A. Modified entropic gravity. *Mod. Phys. Lett. A* **2022**, *37*, 2250186. https://doi.org/10.1142/S0217732322501863.
56. Carroll, S.M.; Remmen, G.N. What is the entropy in entropic gravity? *Physical Review D* **2016**, *93*, 124052, [arXiv:hep-th/1601.07558]. https://doi.org/10.1103/PhysRevD.93.124052.
57. Casini, H. Relative entropy and the Bekenstein bound. *Class. Quant. Grav.* **2008**, *25*, 205021. https://doi.org/10.1088/0264-9381/25/20/205021.
58. Ohya, M.; Petz, D. *Quantum Entropy and Its Use*, 2nd ed.; Springer-Verlag: Heidelberg, 2004.
59. Lashkari, N.; Van Raamsdonk, M. Canonical energy is quantum Fisher information. *Journal of High Energy Physics* **2016**, *2016*, 153, [arXiv:hep-th/1508.00897]. https://doi.org/10.1007/JHEP04(2016)153.
60. Parikh, M.; Sarkar, S.; Svesko, A. Local first law of gravity. *Physical Review D* **2020**, *101*, 104043, [arXiv:gr-qc/1801.07306]. https://doi.org/10.1103/PhysRevD.101.104043.
61. Takesaki, M. *Theory of Operator Algebras I, II, III*; Vol. 124, 125, 127, *Encyclopaedia of Mathematical Sciences*, Springer-Verlag: Berlin, Heidelberg, 2003.
62. Nusbaumer, O. Supplementary Simulation Toolbox for Semiclassical Gravity as Local Statistical Inference. Zenodo, 2026. Zenodo. DOI: 10.5281/zenodo.20090276.
63. Vassilevich, D.V. Heat kernel expansion: user's manual. *Phys. Rep.* **2003**, *388*, 279–360, [hep-th/0306138]. Standard reference for the coefficients of the spectral expansion.
64. Gilkey, P.B. *Invariance Theory, the Heat Equation, and the Atiyah-Singer Index Theorem*, 2nd ed.; CRC Press, 1995.
65. Connes, A. *Noncommutative Geometry*; Academic Press: San Diego, 1994.
66. Chamseddine, A.H.; Connes, A. The Spectral Action Principle. *Commun. Math. Phys.* **1997**, *186*, 731–750, [hep-th/9606001]. Foundational derivation of the Standard Model action from spectral geometry.
67. Faulkner, T.; Guica, M.; Hartman, T.; Myers, R.C.; Van Raamsdonk, M. Gravitation from Entanglement in Holographic CFTs. *JHEP* **2014**, *03*, 051, [1312.7856]. https://doi.org/10.1007/JHEP03(2014)051.
68. Donoghue, J.F. General relativity as an effective field theory: The leading quantum corrections. *Phys. Rev. D* **1994**, *50*, 3874.
69. Di Francesco, P.; Mathieu, P.; Sénéchal, D. *Conformal Field Theory*; Graduate Texts in Contemporary Physics, Springer: New York, 1997. https://doi.org/10.1007/978-1-4612-2256-9.
70. Witten, E. Non-abelian bosonization in two dimensions. *Commun. Math. Phys.* **1984**, *92*, 455–472. https://doi.org/10.1007/BF01215276.
71. Anastasiou, G.; Araya, I.J.; Olea, R. Energy functionals from Conformal Gravity. *Journal of High Energy Physics* **2022**, *2022*, 123, [arXiv:hep-th/2209.02006]. https://doi.org/10.1007/JHEP10(2022)123.
72. Padmanabhan, T. Gravity and quantum theory: Domains of conflict and contact. *International Journal of Modern Physics D* **2020**, *29*, 2030001, [arXiv:gr-qc/1909.02015]. https://doi.org/10.1142/S0218271820300013.
73. Chakraborty, S.; Padmanabhan, T. Thermodynamical interpretation of the geometrical variables associated with null surfaces. *Physical Review D* **2015**, *92*, 104011, [arXiv:gr-qc/1508.04060]. https://doi.org/10.1103/PhysRevD.92.104011.
74. Ali, R.; Xia, T.; Babar, R. First-Order GUP Corrections of Black Hole Thermodynamics in the Framework of $f(R)$ Gravity. *Fortschritte der Physik* **2025**. https://doi.org/10.1002/prop.70017.
75. Bukhari, S.M.A.S.; Pourhassan, B.; Aounallah, H.; Wang, L.G. On the microstructure of higher-dimensional Reissner–Nordström black holes in quantum regime. *Classical and Quantum Gravity* **2023**, *40*, 225007, [arXiv:gr-qc/2304.00940]. https://doi.org/10.1088/1361-6382/acffa0.
76. Breuer, H.P.; Petruccione, F. *The Theory of Open Quantum Systems*; Oxford University Press: Oxford, 2002.

77. Page, D.N. Particle emission rates from a black hole: Massless particles from an uncharged, nonrotating hole. *Phys. Rev. D* **1976**, *13*, 198–206. https://doi.org/10.1103/PhysRevD.13.198.
78. Petz, D. Sufficient subalgebras and the relative entropy of states of a von Neumann algebra. *Communications in Mathematical Physics* **1986**, *105*, 123–131. https://doi.org/10.1007/BF01212345.
79. Aghanim, N.; et al. Planck 2018 results. VI. Cosmological parameters. *Astron. Astrophys.* **2020**, *641*, A6. https://doi.org/10.1051/0004-6361/201833910.
80. BICEP/Keck Collaboration.; Ade, P.A.R.; Ahmed, Z.; Amiri, M.; Barkats, D.; et al. Improved Constraints on Primordial Gravitational Waves using Planck, WMAP, and BICEP/Keck Observations through the 2018 Observing Season. *Phys. Rev. Lett.* **2021**, *127*, 151301, [arXiv:astro-ph.CO/2110.00483]. https://doi.org/10.1103/PhysRevLett.127.151301.
81. Navas, S.; et al. Review of Particle Physics. *Phys. Rev. D* **2024**, *110*, 030001. https://doi.org/10.1103/PhysRevD.110.030001.
82. Abbott, T.M.C.; et al. Dark Energy Survey Year 3 results: Cosmological constraints from galaxy clustering and weak lensing. *Phys. Rev. D* **2022**, *105*, 023520. https://doi.org/10.1103/PhysRevD.105.023520.
83. Famaey, B.; McGaugh, S.S. Modified Newtonian dynamics (MOND): observational phenomenology and relativistic extensions. *Living Rev. Relativ.* **2012**, *15*, 10.
84. Lelli, F.; McGaugh, S.S.; Schombert, J.M.; Pawlowski, M.S. One Law to Rule Them All: The Radial Acceleration Relation of Galaxies. *The Astrophysical Journal* **2017**, *836*, 152, [arXiv:astro-ph.GA/1610.08981]. https://doi.org/10.3847/1538-4357/836/2/152.
85. Buttazzo, D.; Degrassi, G.; Giardino, P.P.; Giudice, G.F.; Sala, F.; Salvio, A.; Strumia, A. Deconstructing the vacuum stability analysis. *JHEP* **2013**, *12*, 089, [arXiv:hep-ph/1307.3536]. https://doi.org/10.1007/JHEP12(2013)089.
86. Morel, L.; Yao, Z.; Cladé, P.; Guellati-Khélifa, S. Determination of the fine-structure constant with an accuracy of 81 parts per trillion. *Nature* **2020**, *588*, 61–65. https://doi.org/10.1038/s41586-020-2964-7.
87. Akrami, Y.; et al. Planck 2018 results. X. Constraints on inflation. *Astron. Astrophys.* **2020**, *641*, A10.
88. Cohen, A.G.; Kaplan, D.B.; Nelson, A.E. Effective field theory, gravity, and the cosmological constant. *Phys. Rev. Lett.* **1999**, *82*, 4971–4974, [hep-th/9803132]. https://doi.org/10.1103/PhysRevLett.82.4971.
89. Li, M. A Model of holographic dark energy. *Phys. Lett. B* **2004**, *603*, 1–5, [hep-th/0403127]. https://doi.org/10.1016/j.physletb.2004.10.014.
90. Linder, E.V. Cosmic growth history and expansion history. *Phys. Rev. D* **2005**, *72*, 043529, [astro-ph/0507263]. https://doi.org/10.1103/PhysRevD.72.043529.
91. Gibbons, G.W.; Hawking, S.W. Cosmological event horizons, thermodynamics, and particle creation. *Phys. Rev. D* **1977**, *15*, 2738.
92. Shannon, C.E. Communication in the Presence of Noise. *Proceedings of the IRE* **1949**, *37*, 10–21. https://doi.org/10.1109/JRPROC.1949.232969.
93. Landauer, R. Irreversibility and Heat Generation in the Computing Process. *IBM J. Res. Dev.* **1961**, *5*, 183–191. https://doi.org/10.1147/rd.53.0183.
94. Weinberg, S. *The Quantum Theory of Fields, Volume 1: Foundations*; Cambridge University Press, 1995.
95. Hoang, A.H. The Top Mass: Interpretation and Theoretical Uncertainties. *Ann. Rev. Nucl. Part. Sci.* **2020**, *70*, 225–255, [arXiv:hep-ph/2004.14831]. https://doi.org/10.1146/annurev-nucl-101918-023530.
96. Degrassi, G.; et al. Higgs mass and vacuum stability in the Standard Model at NNLO. *JHEP* **2012**, *08*, 098.
97. Georgi, H. *Lie algebras in particle physics: from isospin to unified theories*; Westview Press, 1999.
98. Georgi, H.; Glashow, S.L. Unity of All Elementary-Particle Forces. *Phys. Rev. Lett.* **1974**, *32*, 438–441. https://doi.org/10.1103/PhysRevLett.32.438.
99. Weyl, H. Über die asymptotische Verteilung der Eigenwerte. *Nachrichten von der Gesellschaft der Wissenschaften zu Göttingen, Mathematisch-Physikalische Klasse* **1911**, *1911*, 110–117.
100. Bordag, M.; Elizalde, E.; Kirsten, K. Heat kernel coefficients of the Laplace operator on the D-dimensional ball. *J. Math. Phys.* **1996**, *37*, 3713–3729, [hep-th/9503023]. https://doi.org/10.1063/1.531603.
101. Fursaev, D.V.; Patrushev, A.; Solodukhin, S.N. Distributional Geometry of Squashed Cones. *Phys. Rev. D* **2013**, *88*, 044054, [arXiv:hep-th/1306.4000]. https://doi.org/10.1103/PhysRevD.88.044054.
102. Parker, R.H.; Yu, C.; Estey, B.; Müller, H. Measurement of the fine-structure constant as a test of the Standard Model. *Science* **2018**, *360*, 191–195. https://doi.org/10.1126/science.aap7706.

103. Wilson, K.G. Confinement of quarks. *Phys. Rev. D* **1974**, *10*, 2445.
104. Chodos, A.; Jaffe, R.L.; Johnson, K.; Thorn, C.B.; Weisskopf, V.F. New extended model of hadrons. *Phys. Rev. D* **1974**, *9*, 3471–3495. https://doi.org/10.1103/PhysRevD.9.3471.